Icarus 405 (2023) 115699

Contents lists available at ScienceDirect

Icarus

journal homepage: www.elsevier.com/locate/icarus

Internal differentiation and volatile budget of Mercury inferred from the partitioning of heat-producing elements at highly reduced conditions

Hadrien Pirotte [a,*], Camille Cartier [b], Olivier Namur [c], Anne Pommier [d], Yishen Zhang [c], Jasper Berndt [e], Stephan Klemme [e], Bernard Charlier [a]

[a] Department of Geology, University of Liège, 4000 Sart Tilman, Belgium
[b] Centre de Recherches Pétrographiques et Géochimiques, Université de Lorraine, 54501 Vandœuvre-lès-Nancy, France
[c] Department of Earth and Environmental Sciences, KU Leuven, 3001 Leuven, Belgium
[d] Carnegie Institution for Science, Earth and Planets Laboratory, Washington, DC 20015, USA
[e] Institut für Mineralogie, Westfälische Wilhelms-Universität Münster, Münster 48149, Germany

ARTICLE INFO

Keywords:
Mercury
Differentiation
Sulfur
Heat-producing elements
Volatility

ABSTRACT

Understanding the behavior of elements under highly reduced conditions is fundamental to explain the differentiation, crust formation, and volatile budget of Mercury. Here we report experiments on a synthetic composition representative of the bulk silicate Mercury (BSM), at pressure up to 3 GPa, temperature up to 1720 °C, and under highly reduced conditions (~IW − 8 to ~IW − 1, with IW the iron-wüstite oxygen fugacity buffer). We determined partition coefficients for >30 minor and trace elements between silicate melt, metal melt (Fe—Si), sulfide melt (FeS), and MgS solid sulfides. Based on these results and published literature, we modeled the behavior of heat-producing elements (HPE: U, Th, and K) during Mercury's early differentiation and mantle partial melting and estimated their concentrations in the mantle and crust. We found that U, K and especially Th are principally concentrated in the BSM and did not partition into the core because they are not siderophile elements. Uranium is chalcophile under highly reduced conditions, and so our model suggests that an FeS layer at the core-mantle boundary formed during Mercury's primordial differentiation would likely have incorporated large amounts of U, significantly increasing the Th/U ratio of the BSM. However, this is inconsistent with the chondritic or slightly sub-chondritic Th/U ratios of Mercury's lavas. In addition, the likely presence of mantle sulfides, such as MgS, would have also fractionated U and Th, increasing the mantle Th/U. It is possible to have an FeS layer if Mercury formed under less reduced conditions, or if the building blocks of Mercury had Th/U ratios close to the lower end of chondritic data. If, as suggested by our model, no FeS layer formed during differentiation, it means that the majority of HPE are concentrated in Mercury's thin silicate part. Based on the compatibility of U, Th and K, we also show that surface K/Th and K/U ratios are respectively 2–4 times and 3–6 times lower than expected for initial K/Th and K/U ratios similar to enstatite chondrites, implying that the planet suffered an important volatile loss via mechanisms that remain undetermined.

1. Introduction

The partitioning of major and trace elements between silicate, sulfide, and metallic melts strongly depends on the prevailing thermodynamic conditions, particularly oxygen fugacity (fO_2; e.g., Kilburn and Wood, 1997; McCoy et al., 1999; Kiseeva and Wood, 2013, 2015; Wood and Kiseeva, 2015; Namur et al., 2016a; Vander Kaaden and McCubbin, 2016; Wohlers and Wood, 2017; Cartier and Wood, 2019; Steenstra et al., 2020a, 2020b). Investigating the geochemical behavior of elements at various fO_2 conditions is therefore particularly important for understanding the origin and evolution of planets that span a wide range of redox conditions. In particular, Mercury experienced the most reduced conditions among the terrestrial planets of our solar system, with fO_2 expected to be between IW − 7 and IW − 3 (i.e., 7 to 3 log units below the fO_2 of the iron-wüstite equilibrium; McCubbin et al., 2012; Zolotov et al., 2013; Namur et al., 2016a). These peculiar reducing conditions affect elemental partitioning, which itself impacts Mercury's core composition via the incorporation of light elements into liquid iron,

* Corresponding author.
E-mail address: hadrien.pirotte@uliege.be (H. Pirotte).

https://doi.org/10.1016/j.icarus.2023.115699
Received 24 April 2023; Received in revised form 24 June 2023; Accepted 8 July 2023
Available online 10 July 2023

Table 1
Composition of the starting material (in wt%) compared to S-free silicate composition of enstatite chondrites (EH) in the literature.

	This study	Indarch[a]	Indarch[b]	EH[c]
SiO_2	61.26	61.26	67.1	60.83
TiO_2	0.1	0.1	0.05	0.11
Al_2O_3	2.76	2.52	2.18	2.65
Cr_2O_3	0.82	0.82	0.09	0.83
MnO	0.43	0.43	0.26	0.46
MgO	31.37	30.37	27.68	30.48
CaO	1.65	1.65	1.47	2.04
Na_2O	1.55	1.75	1.05	1.57
K_2O	0.19	0.19	0.11	0.17
P_2O_5	0.9	0.9	–	0.84
Total	101.03	100	100	100

[a] Wiik (1956).
[b] Berthet et al. (2009).
[c] Lodders and Fegley (1998).

such as Si (Chabot et al., 2014; Boujibar et al., 2019; Vander Kaaden et al., 2020; Knibbe et al., 2021).

Mercury's density is similar to Earth (~5.43 vs. 5.514 g cm^{-1}), even though the former is much smaller than the latter, with a radius of ~2400 km and ~ 6400 km respectively. On Earth, materials are more compressed in its center (increasing their density) than on Mercury, which means that for Mercury to have a similar density, the planet must have a large metallic core (Ash et al., 1971; Howard et al., 1974; Anderson et al., 1987; Margot et al., 2018). The present-day core is considered to be partially molten (Margot et al., 2007), with a total core radius of ~2000 km (Hauck et al., 2013; Rivoldini and Van Hoolst, 2013) and a solid inner core radius of 0–1600 km (Knibbe and van Westrenen, 2015, 2018; Genova et al., 2019; Knibbe et al., 2021; Goossens et al., 2022). At the pressure of Mercury's core-mantle boundary (CMB, ~5 GPa; Margot et al., 2018; Steinbrügge et al., 2021) a miscibility gap exists in the Fe-Si-S system (Malavergne et al., 2007; Morard and Katsura, 2010); an FeS-rich melt segregates from the coexisting Fe-Si-rich melt at sulfide saturation. Under Mercury's reduced fO_2 conditions, the FeS liquid incorporates a wide array of elements that would otherwise behave as lithophile or siderophile under more oxidized conditions, as on present Earth (Wohlers and Wood, 2015, 2017; Boujibar et al., 2019; Cartier and Wood, 2019; Steenstra et al., 2020a; Wilbur et al., 2022). Therefore, if sulfide saturation occurred during the primordial differentiation of Mercury, its core should be compositionally layered in terms of major and trace elements, including light elements and heat-producing elements. Under highly reduced conditions, sulfur should also be highly soluble in silicate melts (Namur et al., 2016a), consistent with the high sulfur contents of Mercurian lavas (0.5–3.5 wt%; Peplowski et al., 2015; Weider et al., 2015; Namur et al., 2016a). Therefore, Mercury's silicate mantle most likely contains abundant sulfides, probably of the oldhamite (CaS)–niningerite (MgS) series (Namur et al., 2016b; Boukaré et al., 2019; Anzures et al., 2020), which are commonly observed in enstatite chondrites (Crozaz and Lundberg, 1995; Lehner et al., 2013) and are enriched in various trace elements, notably rare-earth elements and actinides (Hammouda et al., 2022) that otherwise behave as lithophile (Ingrao et al., 2019).

Malavergne et al. (2010) first proposed that a solid FeS layer could be stable at the CMB and estimated that it should be <15 km thick if Mercury formed from S-poor Benccubinite chondrites or 100–220 km thick if accreted from S-rich enstatite chondrites. The presence of an FeS layer up to 200 km thick was also proposed based on initial estimates of Mercury's normalized polar moment of inertia using *MESSENGER* gravity measurements (Smith et al., 2012). However, petrological modeling based on sulfur solubility in silicate melt and the Ti contents of Mercury lavas suggests that if an FeS layer exists at the CBM, it must be thinner than 90 km (Namur et al., 2016a; Cartier et al., 2020).

High-spatial resolution measurements by the X-Ray Spectrometer (XRS) onboard *MESSENGER*, which was able to detect fluorescent X-ray emissions from up to ~10 μm of depth (Nittler et al., 2011), were combined in order to map the distributions of Si-normalized major elements (Al, Fe, Mg, Ca, S; Nittler et al., 2018a) and some minor elements, such as Ti (Cartier et al., 2020) and Cr (Nittler et al., 2018b), on the surface of Mercury; lower and upper bounds on Mn concentrations have also been provided (Nittler et al., 2018a). Additional chemical data for O, Na, Cl, K, Th, and U of the surface (up to 100 μm of depth) were acquired at lower spatial resolution by the Gamma-Ray Spectrometer (Peplowski et al., 2011, 2012, 2014; Evans et al., 2012, 2015; McCubbin et al., 2017). New compositional information is expected from the BepiColombo mission. In particular, BepiColombo will measure the concentrations of elements such as P and Ni, as well as heat-producing elements U, Th, and K at higher spatial resolution than *MESSENGER*, using the Mercury Imaging X-ray Spectrometer (MIXS) and the Mercury Gamma ray and Neutron Spectrometer (MGNS) (Bunce et al., 2020; Rothery et al., 2020). These elements are important tracers for investigating the volatile budgets and differentiation histories of terrestrial planets (e.g., McLennan, 2003). In the case of Mercury, it has been suggested that U and K may strongly partition into liquid FeS but not liquid Fe—Si (Wohlers and Wood, 2015, 2017; Boujibar et al., 2019). However, even though Boujibar et al. (2019) recently produced data for U, Th and K partitioning relevant to Mercury's geological context, with a focus on metal/silicate melt partitioning data, data are still scarce at low fO_2 to address key questions regarding the thermochemical evolution of Mercury's interior (Tosi et al., 2013; Boujibar et al., 2019; Boukaré et al., 2019; Peterson et al., 2021).

Here, we report high-pressure and high-temperature experiments on a composition representative of the bulk silicate Mercury (BSM, i.e., the mantle and crust), which we equilibrated with sulfide and metallic melts. We report partitioning data for major, minor, and trace elements between the three melts, and we also present the first data on partitioning between solid MgS and silicate melt. We particularly focus on presenting U, Th and K partition coefficients between FeS and the silicate melt, which complements the data set produced by previous studies, notably Boujibar et al. (2019). These results are used to discuss the distribution of the heat-producing elements (U, Th and K) between Mercury's metallic core, the potential FeS layer at the CMB, and the BSM. We found that the surface Th/U can be used to better constrain the thermodynamic conditions for the formation of an FeS layer. We also discuss the importance of mantle sulfides, such as MgS, for the potential fractionation of U, Th, and K, and their importance for calculating the global volatile budget of Mercury. Our study indicates that it is not possible to reconcile the measured K/Th and K/U surface ratios with a chondritic bulk-composition of Mercury, and the planet must have lost an important fraction of its K.

2. Experimental and analytical methods

2.1. Starting compositions

Mercury's building blocks are often assumed to be compositionally similar to enstatite chondrites (Malavergne et al., 2010, 2014; Zolotov et al., 2013; Cartier and Wood, 2019), and so we synthesized a powder representative of the average silicate portion of enstatite chondrites (Table 1, Wiik, 1956; Lodders and Fegley, 1998; Berthet et al., 2009). Sample synthesis consisted of four steps. (1) High-purity oxides/silicates/phosphate (SiO_2, TiO_2, Al_2O_3, Cr_2O_3, MnO, MgO, $CaSiO_3$, Na_2SiO_3, $K_2Si_4O_9$, $AlPO_4$) were mixed with ethanol in an agate mortar. (2) The powder was then doped with 1000 ppm of U and Th and 500 ppm of other trace elements (Sc, V, Co, Ni, Cu, Zn, Ga, Ge, Rb, Sr, Y, Zr, Nb, Mo, Ce, Nb, Sm, Eu, Gd, Yb, Hf, Ta, and W) using premixed standard solutions. Powders were then dried in an oven at 450 °C overnight. (3) Different amounts of S, FeS, ± CaS were added to the powders to reach sulfide saturation in the silicate melt. In some experiments, only Fe was added to study metal/silicate melt partitioning data in the absence of sulfur. (4) To reduce the oxygen fugacity of the experiments, Si metal

Table 2
Experimental conditions and oxygen fugacity calculated for each experiment.

Run #	T (°C)	P (GPa)	Duration (min)	Source of S*	Phases in quenched silicate melts samples	fO_2[a]	fO_2[b]	fO_2[c]
A022	1620	1.31	60	FeS + Cas	Met	−4.9	−6	
A023	1520	1.31	120	FeS + Cas	Met	−5	−6.4	
A025	1520	1.31	120	CaS	Met	−5.6	−6.8	
A026	1520	1.31	120	FeS + Cas	FeS			−6.5
A027	1520	1.31	120	FeS	FeS, Qtz, Si			−4.7
A038	1620	1.31	45	FeS	FeS, Qtz			−4.7
A039	1620	2	45	FeS	FeS, Qtz, Si			−4.7
A040	1720	1.31	45	FeS	FeS			−4.4
A041	1720	2	45	FeS	FeS, Qtz			−4.5
A042	1620	1.31	45	FeS	Met	−5.5	−6.7	
A043	1620	1.31	45	FeS	FeS			−2.7
B873	1700	3	240	/	Met	−1.9	−1.4	
B875	1700	3	240	/	Met	−4.2	−3.6	
B877	1700	3	240	/	Met	−5	−7	
B879	1700	3	240	FeS	Met + FeS	−4.4	−5.8	−6.7
B880	1700	3	240	/	Met	−5.2	−5.4	
Y037–2	1600	0.1	300	FeS	FeS			−4
Y056–1	1520	0.1	300	FeS	Met + FeS	−4.9	−4	−5.3
Y083–2	1520	0.1	300	FeS	Met + FeS	−4.7	−5.2	−6.4
Y087–2	1520	0.1	300	S	MgS			−8.5

Met = metal, Qtz = quartz, Si = silicon metal. All experiments contain a silicate melt.
* The source of sulfur added in the powder.
[a] Calculated using the Fe-FeO equilibrium.
[b] Calculated using the Si-SiO_2 equilibrium.
[c] Using the equation from Namur et al. (2016a).

was added to the powder. The Si/SiO_2 ratio was balanced accordingly to keep the total Si content of enstatite chondrites. In this way, the total silicon content of the starting material was the same in all experiments but the Si/SiO_2 ratio changed, leading to various fO_2 conditions between experiments (Namur et al., 2016a, 2016b; Anzures et al., 2020). The final powders were dried in an oven at 120 °C and stored in a desiccator until use.

2.2. Experimental methods

Experiments were conducted using a piston-cylinder apparatus and an internally heated pressure vessel (IHPV). Experimental conditions are listed in Table 2. The first set of piston-cylinder experiments (series A) was performed at 1–2 GPa at the University of Liège (Belgium) following the method described in Condamine et al. (2022). We used 0.5″ barium carbonate cells with graphite capsules to maintain intrinsically reduced conditions. Samples were initially pressurized at room temperature to around 0.75 GPa, then heated to 865 °C at a rate of 100 °C/min and held at that temperature for 5 min. During the dwell period, pressure was increased to the target pressure before the sample was heated to the target temperature at a rate of 50 °C/min. The experimental temperature was monitored using a Type-D (W_3-Re_{97}/W_{25}-Re_{75}) thermocouple. Due to the location of the thermocouple tip ~1 mm above the sample, we estimate that the sample was ~20 °C hotter than the temperature measured by the thermocouple, and we reported the corrected temperature in Table 2. The duration of the highest temperature piston-cylinder experiment (1720 °C) was 45 min, and experiments at lower temperatures had durations of 120 min. The experiments were quenched by shutting off the electrical current to the heater. The second set of piston-cylinder experiments (series B) was performed at 3 GPa at the Bayerisches Geoinstitut (BGI, University of Bayreuth) following a procedure similar to that of the University of Liège. In BGI, we however used a talc-Pyrex pressure cell. For these experiments, an outer platinum capsule was used to minimize sulfur and alkali losses.

IHPV experiments (series Y) were performed at 0.1 GPa at the University of Hannover (Germany). Details about the apparatus are available in Berndt et al. (2002) and details about the experimental protocol in Namur et al. (2016a). The powder was loaded into a graphite capsule enclosed in a platinum jacket and placed in the hotspot of the furnace using a 0.1 mm Pt wire. Before heating, the pressure was increased to 0.1 GPa using pure argon as the pressure medium. Two Type-S (Pt/Pt_{90}-Rh_{10}) thermocouples were inserted along the sample to control the heating at the top and bottom of the cell, and two additional Type-S thermocouples were used to monitor the sample temperature. IHPV experiments were conducted at 1520 °C for 300 min, except for experiment Y037–2, which was performed at 1600 °C (Table 2). Experiments were quenched by applying a current to the Pt wire, causing the sample to fall onto a copper plate at ~20 °C at the bottom of the sample holder. Quench rate is expected to be ~100 °C/s down to the glass transition temperature.

2.3. Analytical techniques

Quenched samples were cut in half, mounted in epoxy, and polished for textural and chemical analyses. Samples were dry-polished using SiC pads and diamond powder to avoid sulfide dissolution in the presence of water or other lubricants. Phase determination and description of experimental textures were conducted with a scanning electron microscopy (SEM; FEI Quanta 600, operating at 5 kV accelerating voltage) at the University of Aachen (Germany). Major and minor element concentrations were quantified using a JEOL JXA-8530F electron probe micro-analyzer (EPMA) at the University of Münster (Germany) with a 15 kV accelerating voltage and a 10 nA beam current. On-peak and background analysis times were 15 (10 for Na and K) and 5 s, respectively, for silicate melts and 20 (peak) and 10 (background) s for metals and sulfides. We calibrated Kα X-ray lines with jadeite (Na), olivine (Mg), disthene (Al), hypersthene (Si), pentlandite (Ni), apatite (P), sanidine (K), diopside (Ca), pyrite (S), rutile (Ti), Cr_2O_3 (Cr), rhodonite (Mn), and fayalite (Fe) for silicates, and olivine (Mg), apatite (P), diopside (Ca), pyrite (S), and Si, Ti, Cr, Fe, Mn, and Ni metal standards for metals and sulfides.

Trace element concentrations were analyzed by laser ablation inductively coupled plasma mass spectrometry (LA-ICP-MS) at the University of Münster (Germany) using a Photon Machines (Analyte G2) 193 nm ArF excimer laser (ca. 5 J/cm^2 laser fluence, 10 Hz repetition rate) coupled to a ThermoFisher ElementXR sector field mass spectrometer (MS). The laser spot size was adapted to the size of the phase being analyzed; typical spot diameters were 30–60 μm for silicate glass,

Table 3
Chemical composition of the silicate glass (in wt%).*

Run #	SiO_2	TiO_2	Al_2O_3	Cr_2O_3	MnO	MgO	CaO	FeO	Na_2O	K_2O	P_2O_5	S	Total
Start. Comp	61.26	0.10	2.76	0.82	0.43	31.37	1.65	0.00	1.55	0.19	0.90	0.00	101.03
A022*	57.68	0.01	2.20	0.16	0.29	19.23	11.49	0.28	0.87	0.17	0.01	8.28	100.66
1σ	0.60	0.01	0.04	0.04	0.03	0.42	0.38	0.09	0.05	0.02	0.02	0.30	0.37
A023*	56.55	0.01	3.15	0.17	0.30	18.74	11.89	0.27	1.05	0.14	0.01	8.41	100.70
1σ	0.31	0.01	0.22	0.03	0.03	0.26	0.22	0.04	0.04	0.02	0.01	0.16	0.21
A025*	58.21	0.01	2.27	0.07	0.26	19.22	12.45	0.12	0.68	0.19	0.01	5.80	99.29
1σ	0.28	0.01	0.04	0.03	0.03	0.87	0.41	0.05	0.05	0.02	0.02	0.15	1.26
A026*	53.52	0.01	2.15	0.05	0.13	22.14	13.84	0.32	1.08	0.16	0.40	5.40	99.20
1σ	0.20	0.01	0.05	0.01	0.03	0.13	0.22	0.07	0.04	0.03	0.05	0.08	0.23
A027	63.31	0.07	3.19	0.05	0.12	27.34	1.78	0.55	1.63	0.26	0.01	1.96	100.27
1σ	1.37	0.01	0.21	0.02	0.02	1.43	0.22	0.05	0.13	0.03	0.01	0.20	0.43
A038	70.72	0.02	4.35	0.02	0.07	19.11	1.14	0.26	1.26	0.17	0.01	2.46	99.63
1σ	1.08	0.01	1.08	0.02	0.02	1.51	0.07	0.07	0.17	0.02	0.01	0.14	0.33
A039	61.10	0.03	3.04	0.02	0.09	28.75	1.72	0.52	2.28	0.33	0.00	3.09	100.97
1σ	1.68	0.01	0.17	0.01	0.01	1.63	0.12	0.07	0.38	0.06	0.00	0.13	0.29
A040	73.08	0.02	2.05	0.02	0.10	19.00	1.12	0.28	1.19	0.18	0.01	2.76	99.86
1σ	0.72	0.01	0.03	0.02	0.03	0.57	0.17	0.12	0.20	0.02	0.01	0.07	0.77
A041	68.71	0.02	2.37	0.05	0.13	21.70	1.26	0.46	1.65	0.19	0.00	3.22	99.78
1σ	0.61	0.01	0.04	0.02	0.03	0.47	0.06	0.15	0.31	0.02	0.01	0.07	0.53
A042	59.67	0.11	3.05	0.13	0.47	26.62	1.54	0.13	1.64	0.25	0.00	9.75	103.41
1σ	0.51	0.01	0.04	0.03	0.09	0.32	0.19	0.18	0.10	0.01	0.01	0.34	0.45
A043	69.19	0.08	2.08	0.08	0.16	20.95	1.18	1.14	1.22	0.17	0.27	0.82	97.36
1σ	0.41	0.01	0.03	0.02	0.02	0.21	0.04	0.10	0.03	0.01	0.05	0.05	0.39
B873	55.97	0.13	2.35	0.65	0.38	24.40	1.42	10.57	1.23	0.19	0.16	0.00	97.45
1σ	0.29	0.02	0.09	0.03	0.02	0.51	0.06	0.13	0.10	0.02	0.03	0.00	0.39
B875	64.43	0.17	3.16	0.27	0.45	25.49	1.95	0.71	1.84	0.27	0.01	0.00	98.76
1σ	0.24	0.01	0.08	0.03	0.03	0.49	0.09	0.03	0.10	0.03	0.02	0.01	0.21
B877	53.60	0.07	3.65	0.01	0.07	37.53	2.15	0.18	1.72	0.24	0.02	0.00	99.26
1σ	0.80	0.01	0.33	0.01	0.03	1.77	0.33	0.09	0.33	0.04	0.02	0.01	0.30
B879	54.53	0.02	3.74	0.06	0.24	30.80	1.65	0.58	1.95	0.23	0.01	12.50	106.32
1σ	0.38	0.01	0.16	0.03	0.04	0.66	0.24	0.24	0.13	0.02	0.01	0.30	0.47
B880	63.58	0.15	3.39	0.09	0.37	26.75	2.13	0.18	1.85	0.28	0.01	0.00	98.80
1σ	0.39	0.02	0.11	0.02	0.04	0.73	0.12	0.05	0.26	0.03	0.02	0.01	0.51
Y037-2	63.00	0.10	2.56	0.07	0.12	27.30	1.53	1.08	1.49	0.22	0.02	1.55	99.05
1σ	0.79	0.01	0.05	0.02	0.02	0.40	0.04	0.11	0.04	0.01	0.02	0.04	1.28
Y056-1	61.61	0.06	2.66	0.03	0.11	28.58	1.62	0.35	1.55	0.22	0.02	2.68	99.51
1σ	0.24	0.02	0.04	0.02	0.02	0.11	0.02	0.13	0.06	0.01	0.02	0.05	0.27
Y083-2	60.37	0.06	2.70	0.07	0.15	29.16	1.63	0.40	1.56	0.21	0.00	4.88	101.19
1σ	0.30	0.01	0.04	0.03	0.02	0.22	0.04	0.10	0.04	0.02	0.01	0.10	0.30
Y087-2	52.62	0.13	2.75	0.47	0.37	31.30	1.80	0.03	1.70	0.22	0.03	15.66	107.08
1σ	2.58	0.03	0.14	0.14	0.11	1.75	0.23	0.02	0.08	0.03	0.03	1.25	0.76

The totals above 100% are due to excess calculated oxygen. The first line shows the composition of the starting material (Start. mat.). Fe and S were added in different proportion in the starting material for each experiment (see Table 1).

* CaS doped experiments.

20–60 μm for metals and iron-rich sulfides, and 10–20 μm for MgS. Analytical positions were carefully chosen based on SEM images of the samples to avoid contamination by adjacent phases, and we monitored for contamination by metal inclusions (mainly from small Fe-rich blobs in the silicate glass, see Results) based on the signals (counts per second) of key elements (Si and Fe) in the acquired spectra. Ablated material was transported in a He carrier gas to plasma of the MS. Low-resolution (^{23}Na, ^{27}Al, ^{29}Si, ^{43}Ca, ^{45}Sc, ^{47}Ti, ^{51}V, ^{53}Cr, ^{55}Mn, ^{56}Fe, ^{59}Co, ^{60}Ni, ^{63}Cu, ^{66}Zn, ^{69}Ga, ^{73}Ge, ^{85}Rb, ^{88}Sr, ^{89}Y, ^{90}Zr, ^{93}Nb, ^{95}Mo, ^{137}Ba, ^{140}Ce, ^{146}Nd, ^{147}Sm, ^{153}Eu, ^{157}Gd, ^{172}Yb, ^{178}Hf, ^{181}Ta, ^{182}W, ^{232}Th, ^{238}U) and high-resolution analyses (^{24}Mg, ^{29}Si, ^{31}P, ^{39}K, ^{43}Ca, ^{47}Ti, ^{51}Cr, ^{53}Mn, ^{56}Fe, ^{60}Ni) were performed on each sample. The material was ablated and its composition measured for 40 s after the background was measured for 20 s. We used a washout of 10 s between successive measurements. We did not use a pre-raster of the surface but no obvious surface contamination was observed during the first second of analyses.

Raw trace element data were processed using the GLITTER software (Van Achterbergh et al., 2001; Griffin et al., 2008). Calcium concentrations determined by EPMA were used as an internal standard for silicate glass analyses, whereas those of iron were used for sulfide and metallic melt analyses. We used the NIST 612 reference material for silicates, and BHVO-2G basalt for sulfides and metals; using this Fe-rich basalt produced data more consistent with the microprobe data than using NIST 612 for FeS and Fe—Si.

2.4. Oxygen fugacity estimates

The oxygen fugacity (fO_2) of the samples can be estimated from the FeO content of the silicate melt and the Fe content of the metallic melt following the thermodynamic equilibrium between iron and wüstite:

$$Fe^{Met} + \frac{1}{2}O_2 = FeO^{Sil} \quad (1)$$

where the superscripts 'Met' and 'Sil' indicate metallic and silicate melts, respectively. However, under reducing conditions, the silicate melt FeO content is too low (Table 3) to be accurately measured, leading to large errors when estimating fO_2 (Cartier et al., 2014; Namur et al., 2016a). We therefore used the equilibrium reaction (Cartier et al., 2014):

$$Si^{Met} + O_2 = SiO_2{}^{Sil} \quad (2)$$

Oxygen fugacity was calculated by considering the effects of temperature and pressure, and is expressed as the difference relative to the IW buffer (in bar). We consider ideality in our calculations. All details on the calculation methods, including the calculation of ΔIW at high-pressure, are available in Namur et al. (2016a). We estimate that errors on fO_2 calculations are ~0.5 log units (Namur et al., 2016a).

Some of the sulfide-saturated experiments did not contain a metal phase, and we could not use silicate-metal equilibrium to calculate fO_2.

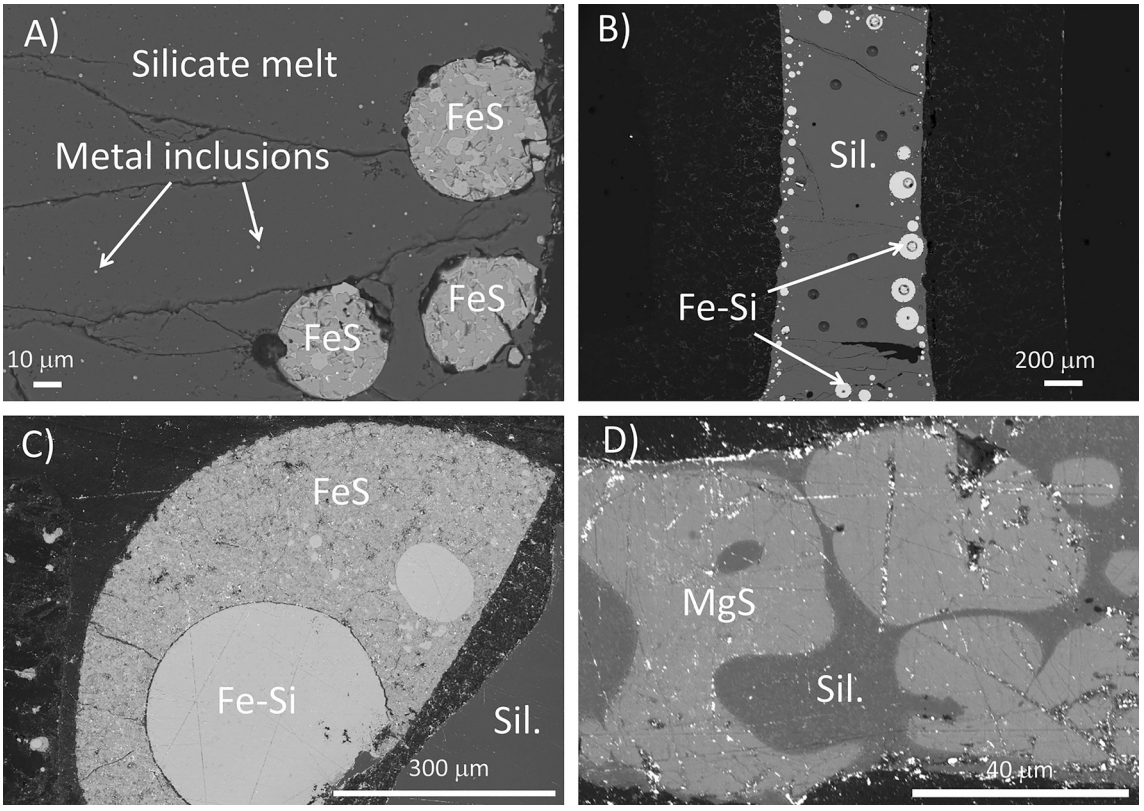

Fig. 1. Back-scattered electron images of selected quenched samples. (a) Metal inclusions in the silicate glass and Fe inclusions in FeS (experiment A040). (b) Large (≥50 µm) globules of Fe—Si in FeS-free experiment A042. We were able to perform large laser points on those. (c) Fe—Si globules surrounded by FeS due to their immiscibility (experiment Y083–2). Smaller Fe—Si globules are also present in the FeS. They were avoided during analyses for both EPMA and LA-ICP-MS. (d) MgS sulfide crystals in an Fe-free IHPV experiment (experiment Y087–2).

For those experiments, we used the following empirical equation linking the S content in the silicate melt to fO_2 (Namur et al., 2016a):

$$ln[S]_{SCSS} = a + b\frac{1}{T} + c\frac{P}{T} + dlogfO_2 + \sum e_i \frac{X_i}{X_{SiO_2}} \quad (3)$$

where $[S]_{SCSS}$ is the sulfur content at sulfide saturation (SCSS, wt%) in the silicate melt, T is temperature (K), P is pressure (bar), fO_2 is oxygen fugacity (bar), a, b, c, d and e_i are regression coefficients, and X_i is the mole fraction of oxide i in the melt, recalculated on a sulfur-free basis (Namur et al., 2016a). We estimate that errors using this method are ~1 log unit. We also used this equation to calculate fO_2 for some sulfide-saturated experiments from the literature with anomalously high Si contents (>20 wt%) in the metal phase and low $[S]_{SCSS}$ (<2 wt%).

Table 4
Major and minor elements composition of metals (in wt%).

Run #	Si	Ti	Cr	Mn	Ca	Ni	Fe	P	S	Total
A022	13.81	0.01	2.33	0.02	0.02	0.30	77.84	2.11	0.04	96.49
1σ	0.32	0.01	0.08	0.01	0.02	0.02	0.35	0.16	0.02	0.32
A023	12.83	0.03	2.25	0.03	0.04	0.31	78.41	1.93	0.13	95.95
1σ	0.44	0.07	0.18	0.03	0.04	0.04	2.64	0.39	0.33	2.15
A025	16.78	0.02	2.31	0.23	0.02	0.19	75.25	1.81	0.01	96.62
1σ	0.24	0.02	0.11	0.03	0.02	0.05	0.38	0.17	0.01	0.36
A042	21.28	0.07	1.87	0.16	0.00	0.12	73.27	1.11	0.00	97.88
1σ	0.26	0.01	0.07	0.02	0.00	0.02	0.38	0.07	0.00	0.31
B873	0.01	0.00	0.17	0.00	0.01	0.10	89.09	2.42	0.03	91.83
1σ	0.01	0.00	0.05	0.01	0.01	0.03	0.47	0.44	0.01	0.42
B875	1.22	0.01	2.06	0.08	0.00	0.11	87.41	1.50	0.04	92.44
1σ	0.18	0.01	0.04	0.04	0.01	0.05	0.35	0.17	0.03	0.28
B877	26.31	0.24	2.35	1.28	0.01	0.13	67.54	1.09	0.00	98.95
1σ	1.07	0.03	0.22	0.07	0.01	0.02	1.12	0.22	0.00	0.57
B879	14.95	0.00	0.03	0.00	0.00	0.13	82.90	0.91	0.31	99.25
1σ	0.95	0.01	0.01	0.00	0.01	0.03	0.84	0.08	0.08	0.30
B880	10.60	0.04	2.39	0.41	0.00	0.15	80.48	1.25	0.01	95.34
1σ	0.36	0.01	0.07	0.02	0.00	0.03	1.12	0.08	0.01	1.16
Y056-1	0.85	0.01	0.09	0.02	0.00	0.21	90.60	1.98	0.92	94.69
1σ	0.47	0.01	0.10	0.05	0.01	0.07	3.19	1.00	1.78	1.79
Y083-2	5.27	0.01	0.24	0.02	0.01	0.16	89.05	1.89	0.49	97.14
1σ	1.72	0.01	0.09	0.02	0.01	0.05	2.07	0.65	0.30	0.57

Low totals are explained by the incorporation of minor/trace elements not measured using the electron microprobe, and notably carbon.

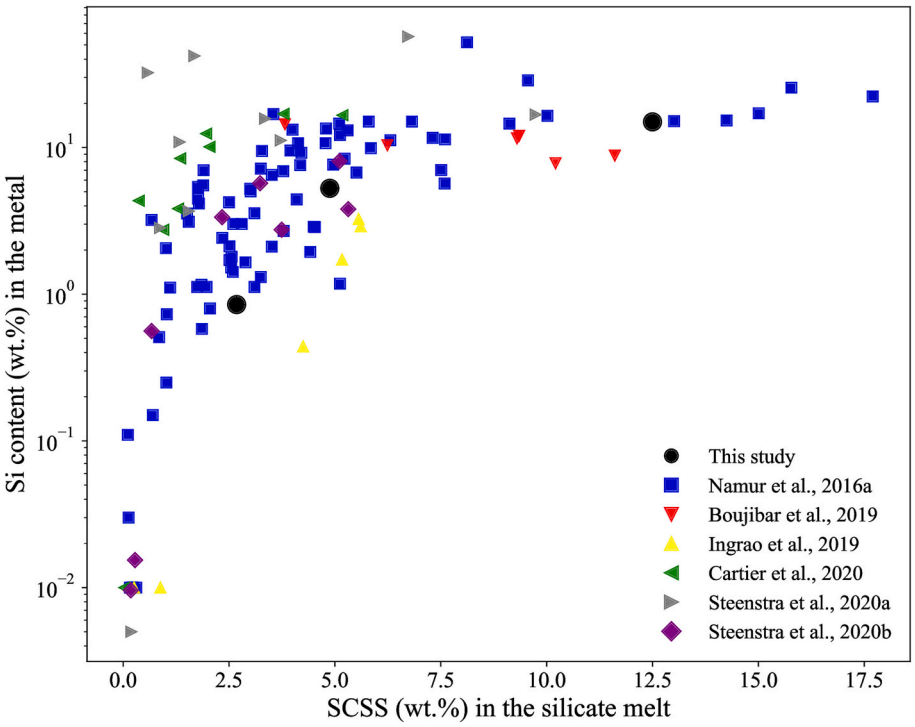

Fig. 2. Si content in metal phases vs. sulfur content at sulfide saturation (SCSS) in the silicate melt. The SCSS corresponds to the maximum solubility of sulfur in a silicate melt at saturation. These two measures are positively correlated because they are linked by the oxygen fugacity.

Comparison between fO_2 calculation methods can be found in the supplementary materials. Oxygen fugacity estimates for our experiments range from IW − 8.5 to IW − 1.4. The most reduced experiment contains solid MgS (Table 2).

3. Results

3.1. Attainment of equilibrium

The attainment of equilibrium in our experiments is supported by several observations. First, the duration of our experiments is similar to that of previous experiments performed on similar compositions (e.g., Wohlers and Wood, 2017; Boujibar et al., 2019; Steenstra et al., 2020a, 2020b) and well above the duration needed to attain equilibrium, as estimated by Thibault and Walter (1995) and Corgne et al. (2008). Second, optical observations and the measured chemical compositions reveal a homogeneous silicate melt phase in all samples. We explained the presence of Si blobs surrounded by SiO_2 in two of our experiments (A027 and A039) by the shielding of Si by stable SiO_2 phase, leading to uncomplete Si oxidation. Third, our partition coefficient data are in good agreement with previous studies where thermodynamic equilibrium was reached (e.g., Cartier et al., 2014; Wohlers and Wood, 2015,

Table 5
Major and minor elements composition of sulfides (in wt%).

Run #	Si	Ti	Cr	Mn	Mg	Ca	Ni	Fe	S	Total
A026	0.01	0.16	4.17	0.99	0.12	0.03	0.10	54.81	37.14	97.58
1σ	0.00	0.02	0.15	0.04	0.02	0.02	0.02	0.22	0.13	0.39
A027	0.04	0.31	2.78	1.12	0.10	0.01	0.01	57.01	36.99	98.38
1σ	0.01	0.04	0.37	0.08	0.01	0.01	0.02	0.36	0.08	0.15
A038	0.01	0.30	2.31	0.81	0.15	0.01	0.03	57.96	36.61	98.20
1σ	0.01	0.13	0.49	0.13	0.04	0.01	0.01	0.77	0.27	0.32
A039	0.09	0.18	1.44	0.83	0.15	0.01	0.03	58.67	36.23	97.66
1σ	0.15	0.07	0.41	0.05	0.06	0.01	0.02	0.84	0.24	0.59
A040	0.01	0.24	1.73	0.76	0.16	0.02	0.03	58.87	36.16	97.99
1σ	0.00	0.07	0.30	0.05	0.03	0.02	0.01	0.58	0.58	0.49
A041	0.02	0.39	2.56	0.91	0.14	0.00	0.02	57.32	36.50	97.88
1σ	0.01	0.13	0.29	0.10	0.03	0.00	0.02	0.61	0.39	0.59
A043	0.01	0.03	1.63	0.62	0.01	0.00	0.03	59.26	36.41	98.04
1σ	0.01	0.02	0.25	0.05	0.01	0.00	0.02	0.42	0.13	0.33
B879	0.04	0.35	2.68	0.47	0.18	0.01	0.01	57.70	37.29	98.74
1σ	0.04	0.20	0.69	0.10	0.05	0.01	0.01	1.16	0.34	0.44
Y037–2	0.00	0.09	2.06	0.87	0.28	0.01	0.04	58.96	37.26	99.57
1σ	0.00	0.02	0.25	0.02	0.04	0.01	0.02	0.45	0.06	0.29
Y056–1	0.01	0.18	1.69	0.75	0.13	0.02	0.02	59.13	37.08	99.01
1σ	0.01	0.12	0.67	0.10	0.03	0.02	0.01	0.83	0.27	0.37
Y083–2	0.01	0.64	3.86	0.93	0.22	0.01	0.02	56.57	37.34	99.61
1σ	0.01	0.30	0.75	0.04	0.02	0.01	0.01	1.29	0.09	0.23
Y087–2	0.02	0.41	3.81	4.46	35.19	0.85	0.02	0.29	54.17	99.23
1σ	0.01	0.03	0.66	0.42	0.83	0.03	0.01	0.02	0.31	0.11

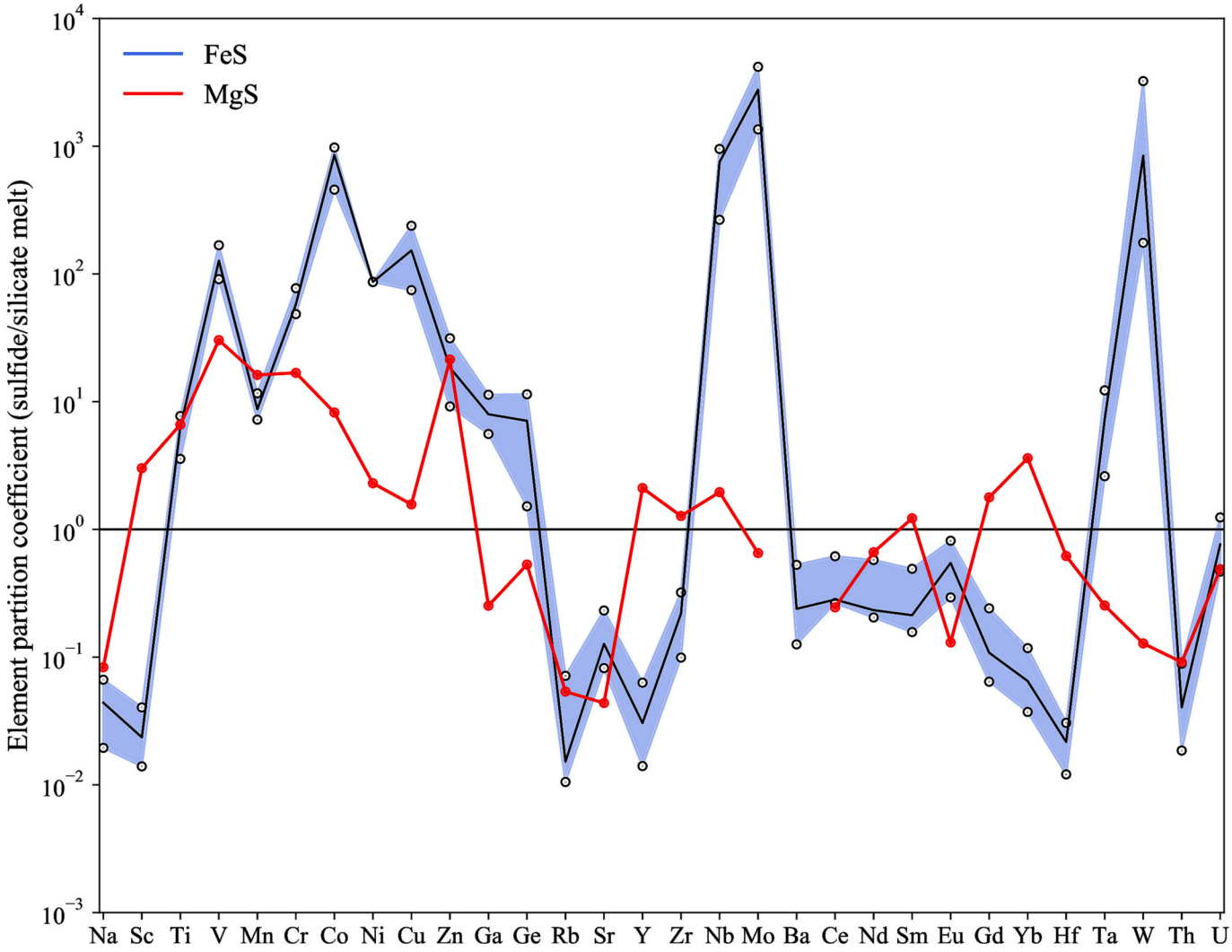

Fig. 3. Elemental sulfide/silicate partition coefficients. Elements are sorted by increasing atomic number. The blue line shows the median values of FeS/silicate melt partition coefficients from experiments between IW− 6 and IW − 4. The blue shaded area indicates the ±95% confidence interval for each element. The red line shows the data from MgS/silicate partitioning. There is no confidence interval as only one experiment contained MgS. The black horizontal line marks D = 1, i.e., the element partitions equally between the silicate melt and sulfides.(For interpretation of the references to colour in this figure legend, the reader is referred to the web version of this article.)

2017; Ingrao et al., 2019; Steenstra et al., 2020a, 2020b).

3.2. Phase assemblages and textural analyses

Some samples (B879, Y056–1, Y083–2) contain three equilibrated melts (silicate melt quenched to glass, metallic melt, and sulfide melt), but most experiments contain either equilibrated FeS and silicate melts without Fe—Si metal or equilibrated Fe—Si and silicate melts without FeS (Table 2). Backscattered electron images of selected samples are presented in Fig. 1. Large FeS globules (>100 μm in diameter) are circular and usually host small Fe—Si globules (Fig. 1c) which result from the miscibility gap in the Fe-S-Si system at the pressure and temperature conditions of our experiments (Malavergne et al., 2007; Morard and Katsura, 2010). Fe—Si metal globules, when present, are mostly spherical and can exceed 100 μm in diameter (Fig. 1b, c). Regardless of whether or not experiments contain large metal globules, some small (<10 μm diameter) Fe droplets and (Fe,Ca,Mg)S blobs are observed in the FeS phase, both probably forming by exsolution during the quench (Fig. 1c). In the Fe-free IHPV experiment (Table 2: Y087–2; Fig. 1d), the only sulfide phase is pure MgS, which occurred as 30–40 μm in width blobs with smooth and irregular contours. MgS was likely a solid phase, because the experiment was performed well below (1520 °C) their very high melting temperature (~2200 °C, Jantzen et al., 2017). In several experiments, the silicate glass contains micro-globules (<1 μm) of metal comparable to those described in previous studies (Fig. 1a: Boujibar et al., 2014; Malavergne et al., 2014). These inclusions are thought to be formed during quench (Boujibar et al., 2014). Quartz grains are sometimes present in the quenched samples, they are most commonly circular and, in some experiments (A027 and A039), they locally enclosed silicon metal, suggesting incomplete Si oxygenation due to SiO_2 shielding, as explained in Section 3.1.

3.3. Major and minor element compositions

In most experiments, the composition of the silicate melt is relatively similar to that of the starting material (Table 3). The SiO_2 content of the glass varies from 55 to 70 wt% but is typically around 60 wt%. The MgO content varies from 20 to 30 wt% and the Al_2O_3 content is around 2 wt %. CaO content in the glass is between ~1 and ~ 2 wt%, except in the CaS-doped experiments (A022, A023, A025 and A026) in which CaO content reaches values from ~11 to ~14 wt%. The highest S content in the quenched glass in all experiments is about 15 wt%, but most samples

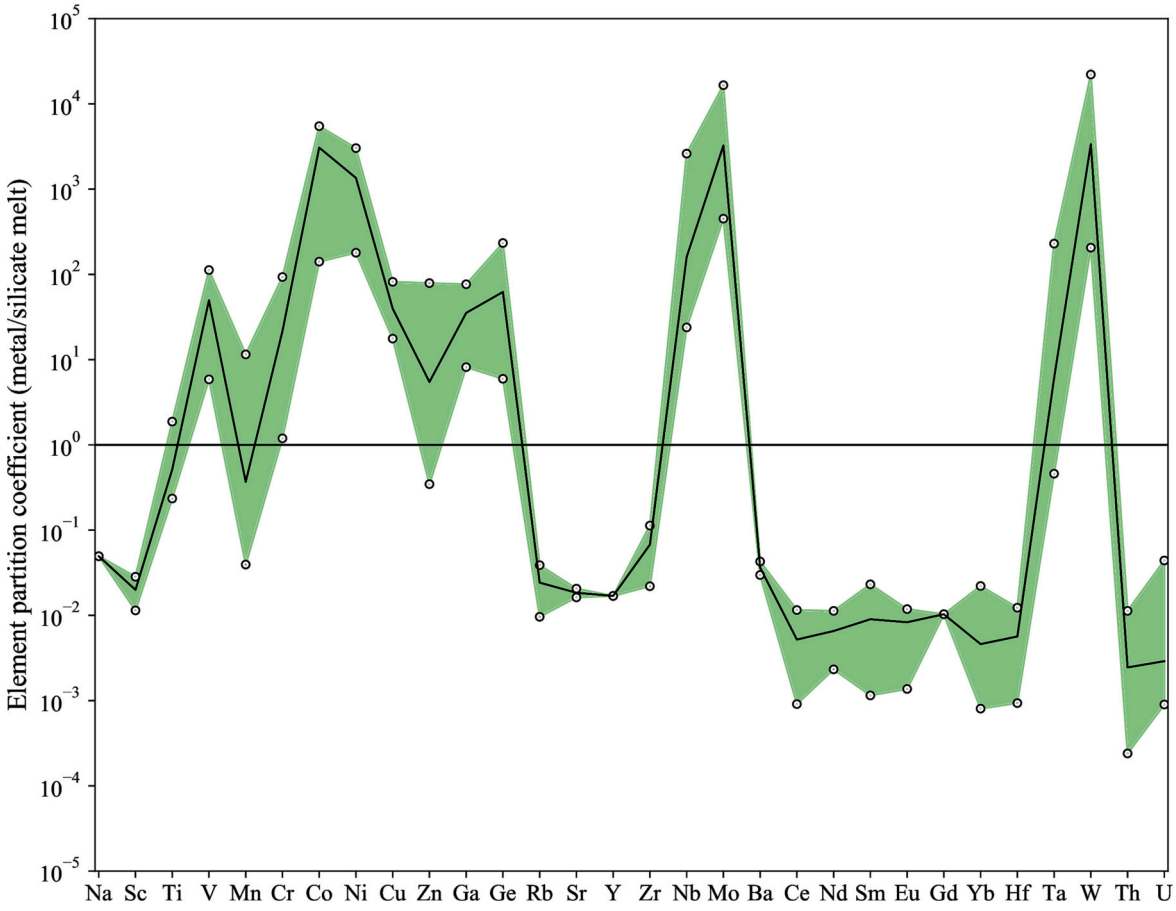

Fig. 4. Element metal/silicate partition coefficients. Elements are sorted by increasing atomic number. The black line shows the median values of metal/silicate melt partition coefficients from experiments between IW − 7 and IW − 1. The green shaded area represents the ±95% confidence interval for each element. The horizontal line shows D = 1, i.e., the element partitions equally between the silicate melt and the metal. (For interpretation of the references to colour in this figure legend, the reader is referred to the web version of this article.)

contain <10 wt% S. Variable S contents are mostly responsible for the observed variations in the other elemental contents. Glass FeO contents are generally low (<1 wt%), except for experiment B873 (>10 wt%). Glasses in all experiments have similar alkali contents of ~1.5 wt% Na_2O and ~ 0.2 wt% K_2O.

Metallic phases are dominated by an iron-silicon alloy containing 1–25 wt% Si (Table 4). Chromium and nickel are minor components (up to 2 wt% for Cr and around ~0.2 wt% for Ni). Phosphorous is also a minor component in the metallic phases (≤ 2.4 wt%). At the investigated pressures of our experiments (≤3 GPa), there is a miscibility gap in the Fe-Si-S system and almost no S is present in the metal (<1 wt%). The S content in the silicate melt is positively correlated with the silicon content in the metal (Fig. 2), consistent with previous works showing that both Si and S are controlled by fO_2 (e.g., Cartier et al., 2014; Cartier and Wood, 2019).

Sulfide melt compositions are mostly composed of Fe and S, with up to 5 wt% Cr and Mn substituting for Fe (Table 5). The S contents of FeS phases are constant at around 37 wt%, corresponding to stoichiometric FeS. This indicates that there is no oxygen (i.e. another −2 anion) in the FeS globules. FeS globules are quenched liquids because all experiments were performed significantly above the FeS liquidus at the investigated pressures (e.g., Chen et al., 2008). Pure solid MgS is only observed in the iron-free experiment Y087–2, quenched at 0.1 GPa and 1520 °C (Table 5).

3.4. Trace element partitioning between sulfides (FeS and MgS) and the silicate melt

The partition coefficient D of an element M between phases A (FeS sulfide; or MgS sulfide) and B (silicate melt) is defined as:

$$D_M^{A/B} = C_M^A / C_M^B \quad (4)$$

where C_M^A and C_M^B are the concentrations of element M in phases A and B (in wt%), respectively. Our results show that most transition metals (V, Cr, Mn, Co, Ni, Cu, Nb, Mo, Ta, W) present a strong affinity for FeS (Fig. 3). Except for Ti, which mainly partitions into FeS at ≤IW − 4, group 3 and 4 transition metals (Sc, Y, Zr, Hf) remain strongly lithophile. Zn, Ga, and Ge also strongly partition into FeS (Fig. 3). Lanthanides are strongly lithophile even under very reduced conditions, except for Eu, which has a stronger affinity for FeS (Fig. 3). In contrast, Eu partitions less into MgS than the other lanthanides (Fig. 3, $D^{MgS/silicate\ melt} \sim 0.1$ for Eu, while it increases from 0.25 for Ce to 1.75 for Yb). Alkali metals and alkaline earth metals are also mostly lithophile (Fig. 3). Actinides (U and Th) are both lithophile, although U partitions more strongly into FeS and MgS than Th.

We investigated trace element partitioning between MgS and the silicate melt in a single experiment. We observe significant differences between the partitioning behavior of trace elements in MgS and in FeS. Athough the observed differences are probably mainly related to the phase composition (MgS vs. FeS), they also result from the physical state of the phase (solid for MgS vs. liquid for FeS) and the experimental fO_2. Indeed, the only experiment containing MgS was at ~IW − 8.5,

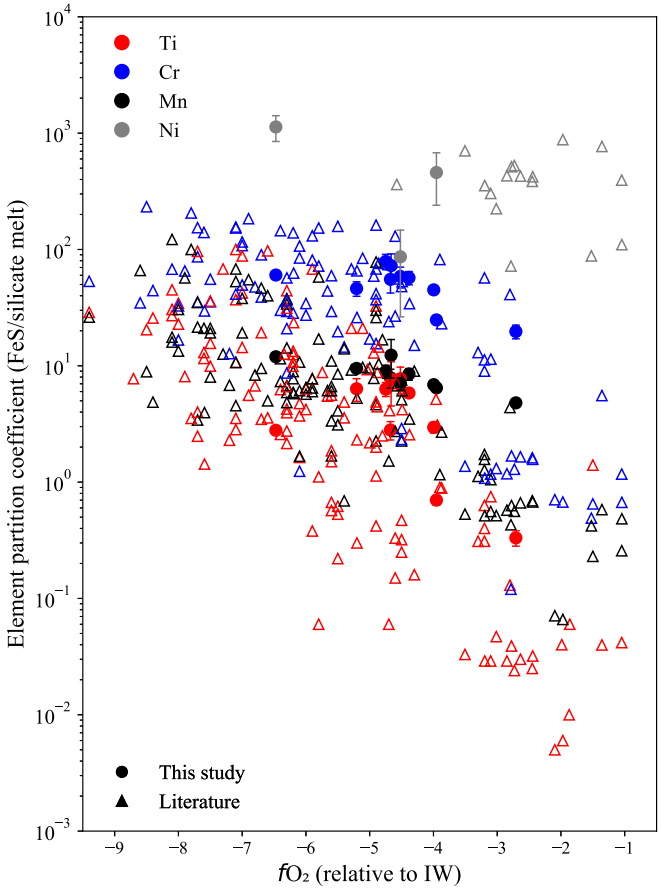

Fig. 5. FeS/silicate melt partition coefficients for Ti, Cr, Mn, and Ni as a function of oxygen fugacity. Element affinities for FeS exponentially increase with decreasing oxygen fugacity. Error bars are shown for partition coefficients from this study. Literature data are from Namur et al. (2016a), Cartier et al. (2020), Steenstra et al. (2020a, 2020b).

significantly more reduced than experiments containing FeS (IW-2.7 to IW − 6.7). Nonetheless, our results tentatively show that $D^{MgS/silicate} > D^{FeS/silicate}$ for Sc, Ti, Y, Zr, and Hf (with $D^{MgS/silicate} > 1$ for those elements, except for Hf), whereas $D^{MgS/silicate} < D^{FeS/silicate}$ for all other transition metals as well as Zn, Ga, and Ge. MgS also incorporates less U ($D_U^{MgS/silicate} \approx 0.5$) and Th ($D_{Th}^{MgS/silicate} \approx 0.1$) than FeS. In FeS, lanthanides are characterized by a decrease in $D^{FeS/silicate}$ with increasing atomic weight (Fig. 3), whereas they behave oppositely in MgS (this study), CaS (Ingrao et al., 2019), and (Ca,Mg)S (Dickinson et al., 1990). We also observed a positive Eu anomaly in FeS and CaS (Ingrao et al., 2019), but none in MgS (this study) or (Ca,Mg)S, as previously observed by Dickinson et al. (1990).

3.5. Metal/silicate trace element partitioning

Under the reduced conditions of our experiments, most transition metals (V, Cr, Co, Ni, Cu, Nb, Mo, W) have always a strong affinity for metals (Fig. 4), while Mn and Ta have their $D^{metal/silicate} > 1$ only at low fO_2. However, transition metals from groups 3 and 4 (Sc, Y, Zr, Hf) are lithophile, except for Ti, whose $D^{metal/silicate} > 1$ at lower fO_2 (Figs. 4 and 5). Zn, Ga, and Ge are incorporated into metals, lanthanides are strongly lithophile ($D^{metal/silicate} < 0.1$), and actinides (U and Th) are also strongly lithophile, with $D_U^{metal/silicate} < 0.05$ and $D_{Th}^{metal/silicate} < 0.01$ (Fig. 4).

4. Discussion

4.1. The effect of fO_2 on elemental partitioning

In order to apply our results to Mercury's primordial evolution, we focus here on the elements that were measured by *MESSENGER* (Ti, Cr, Mn, K, Th, U) or are likely to be measured by BepiColombo (e.g., Ni; Benkhoff et al., 2010). D values for all the other measured elements are however provided in the supplementary material.

As oxygen fugacity decreases, many elements become less lithophile and increasingly chalcophile and/or siderophile (Wohlers and Wood, 2015, 2017; Wood and Kiseeva, 2015; Vander Kaaden and McCubbin, 2016; Namur et al., 2016a; Ingrao et al., 2019; Boujibar et al., 2019; Cartier et al., 2020; Steenstra et al., 2020a, 2020b). As illustrated in Figs. 3 and 4, most transition metals are chalcophile/siderophile under Mercurian conditions, and their partitioning behavior strongly depends on fO_2. All experiments from the literature had their fO_2 recalculated following the method described above (Section 2.4). Ti starts being majorly incorporated into FeS at around IW − 4 and below, whereas Cr, Mn, and Ni are always strongly incorporated into sulfides under such conditions (Fig. 5). Mn is 5 to 10 times less incorporated into FeS than Cr, and Ni has the most affinity with FeS of these four elements (Fig. 5). These elements also become highly incorporated into metals under reducing conditions, with Cr and Ni having the most affinity, followed by Mn and Ti.

Our data show that U and Th become less lithophile as oxygen fugacity decreases (Fig. 6, left panel), with values of $D_U^{FeS/silicate}$ ranging from ~10^{-2} to 1 and of $D_{Th}^{FeS/silicate}$ from ~10^{-3} to 10^{-1} for IW-2 to IW-6. Th remains lithophile at all fO_2 values investigated here, and is ~20 times less chalcophile than U. These partitioning data are in good agreement with the literature (e.g., Wohlers and Wood, 2015, 2017; Boujibar et al., 2019; Steenstra et al., 2020b). There is no clear trend for U and Th partitioning between metal and silicate with the fO_2 (Fig. 6, right panel). U and Th partition only slightly into the Fe—Si metal, even under very reducing conditions, with $D_U^{metal/silicate} <$ ~0.1, with the exception of one value from Malavergne et al., 2007, and $D_{Th}^{metal/silicate} <$ ~0.01. Based on our results and previous data (Chabot and Drake, 1999; Corgne et al., 2007; Mills et al., 2007; Bouhifd et al., 2007, 2013; Steenstra et al., 2018; Boujibar et al., 2019), $D_K^{FeS/silicate}$ has a fairly constant partition coefficient value over the entire range of oxygen fugacity considered, with a median value of ~0.06 and a standard deviation of ~0.13 when excluding the data from Chabot and Drake (1999), which show anomalous high partition coefficients for K (Fig. 6, left panel). For metal-silicate partitioning, K shows an increasing siderophile behavior as oxygen fugacity decreases (Fig. 6, right panel).

4.2. Parameterization of U, Th, and K partition coefficients

Given the relative abundance of partitioning data for U and Th at low fO_2 conditions, we parameterized FeS/silicate melt partitioning using a least squares regression. The partition coefficients can be modeled as a function of fO_2 using the following equation

$$ln(D_X) = a + blog(fO_2) \quad (5)$$

The regression coefficients and their uncertainties are reported in Table 6. Temperature was found not to be a significant parameter for the regression. To parameterize the behavior of U and Th between FeS and silicate melt, we selected samples with $D_U^{FeS/silicate} > 0.001$ and $D_{Th}^{FeS/silicate} > 0.0001$ because considering smaller values provided unsatisfactory parameterization, especially for U. This observation may be due to the difficulty to measure such low U concentrations and/or to a change in the partitioning behavior of U at higher fO_2.

Based on a dataset of 53 measurements, we find a very strong correlation ($R^2 = 0.942$) between $D_U^{FeS/silicate}$ and $D_{Th}^{FeS/silicate}$:

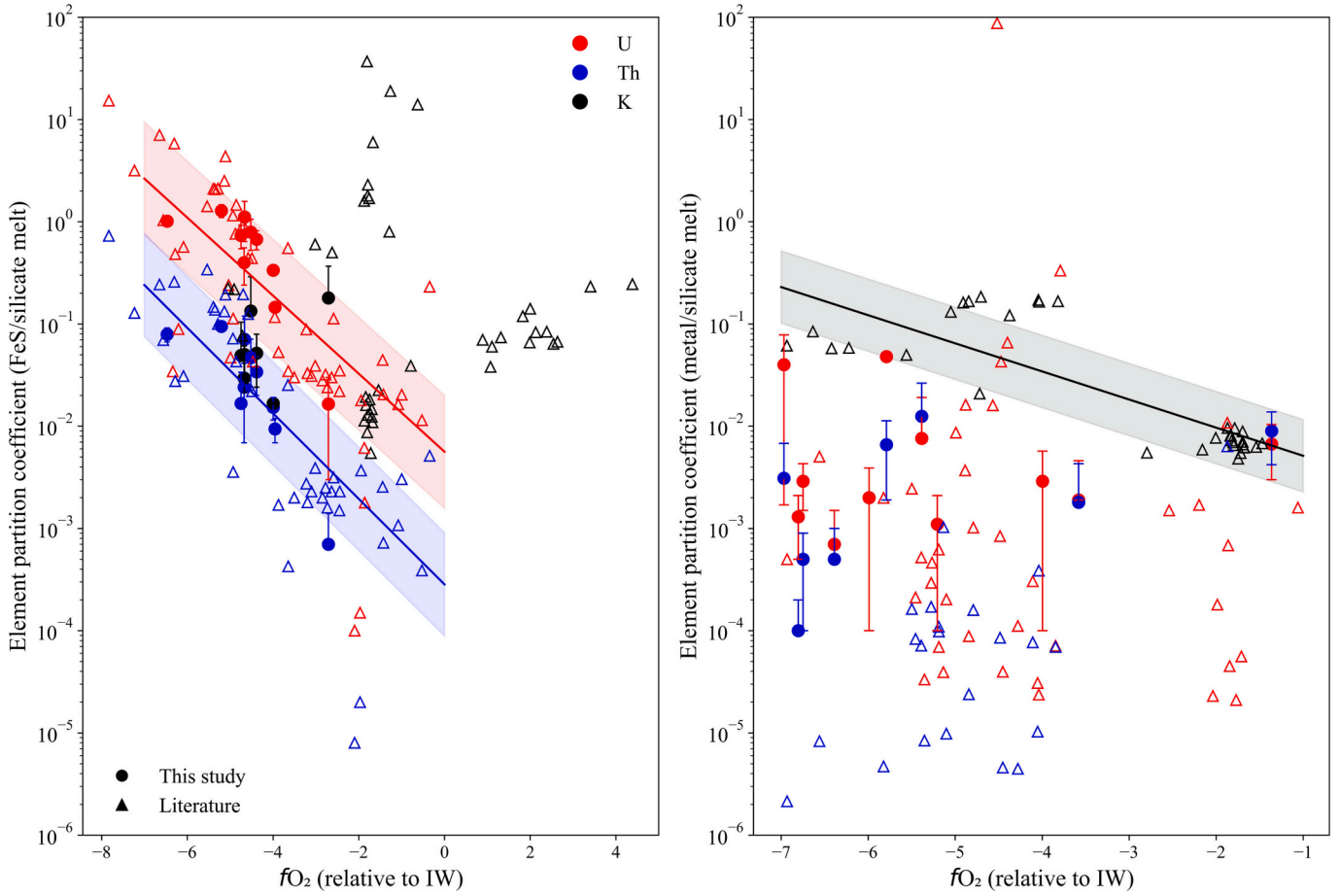

Fig. 6. Left panel: FeS/silicate melt partition coefficients for U, Th, and K as a function of oxygen fugacity. U and Th become increasingly chalcophile with decreasing oxygen fugacity but D_U/D_{Th} stays constant at ~20. Right panel: Metal/silicate melt partition coefficients for U, Th, and K as a function of oxygen fugacity. No clear trend can be seen between partition coefficients and fO_2 for U and Th. K seems to be more siderophile with decreasing oxygen fugacity. Error bars are shown for partition coefficients from this study. Regression lines for $D_U^{FeS/silicate}$, $D_{Th}^{FeS/silicate}$ and and $D_K^{metal/silicate}$ were calculated from Eq. (5) in the following section (4.2, Parameterization of U, Th, and K partition coefficients). The colored areas are the 1 s interval of confidence. Literature data for the left panel are from: Chabot and Drake (1999), Bouhifd et al. (2007), Corgne et al. (2007), Malavergne et al. (2007), Mills et al. (2007), Cartier (2014), Wohlers and Wood (2015), Wohlers and Wood (2017), Boujibar et al. (2019) and Steenstra et al. (2020b). Literature data for the right panel are from Bouhifd et al. (2007), Corgne et al. (2007), Malavergne et al. (2007), Bouhifd et al. (2013), Cartier (2014), Wohlers and Wood (2017), Boujibar et al. (2019).

Table 6
Coefficients of regression for Eqs. (5)–(7).

Eq. (5)	a	b	R^2	F	n
$D_U^{FeS/Silicate\ melt}$	−5.1788	−0.8785	0.62	92.98	59
Standard error	0.403	0.091			
$D_{Th}^{FeS/Silicate\ melt}$	−8.167	−0.9629	0.685	106.7	51
Standard error	0.41	0.093			
$D_K^{Metal/Silicate\ melt}$	−5.9038	−0.6332	0.672	63.59	33
Standard error	0.294	0.079			
Eq. (6)	a	b	R^2	F	n
$D_U^{FeS/Silicate\ melt}$	2.732	0.9763	0.942	827.3	53
Standard error	0.174	0.034			
Eq. (7)	a	b	R^2	F	n
$D_{Th}^{Metal/Silicate\ melt}$	−3.278	0.6568	0.523	23.04	23
Standard error	1.03	0.137			

R^2 is the coefficient of determination, F is the score of a F-test for a significant linear regression between the response variable and the predictor variables, and n is the number of observations.

$$ln\left(D_U^{FeS/silicate}\right) = 2.7320 + 0.9763 ln\left(D_{Th}^{FeS/silicate}\right) \quad (6)$$

This regression allows the modeling of the evolution of the Th/U ratio during Mercury's differentiation, even if the absolute concentrations of U and Th in different reservoirs might be imprecise due to the uncertainties of Eq. (5) ($R^2 < 0.7$; Table 6). No parameterization was obtained for $D_K^{FeS/silicate}$ with fO_2. As seen in Section 4.1 (Fig. 6, left panel), $D_K^{FeS/silicate}$ is somewhat constant at around ~0.06 for any fO_2 considered in this study or the literature.

We observe no clear correlation between $D_U^{metal/silicate}$ or $D_{Th}^{metal/silicate}$ and fO_2 (Fig. 6, right panel). $D_U^{metal/silicate}$ seems correlated with pressure, but the available data are insufficient to obtain a statistically meaningful regression. Similarly, it was not possible to obtain a satisfying parametrization for $D_{Th}^{metal/silicate}$. As observed with $D_U^{FeS/silicate}$ and $D_{Th}^{FeS/silicate}$, there is a correlation between $D_U^{metal/silicate}$ and $D_{Th}^{metal/silicate}$. Although the error is large, we can nonetheless express the relation as:

$$ln\left(D_{Th}^{metal/silicate}\right) = -3.2780 + 0.6568 ln\left(D_U^{metal/silicate}\right) \quad (7)$$

with $R^2 = 0.523$ (Table 6) with 23 data points, restricted to $D_{Th}^{metal/silicate} > 10^{-5}$. It was possible to parameterize $D_K^{metal/silicate}$ with oxygen fugacity using Eq. (5), with a R^2 of 0.672 using 33 samples. Standard errors are listed in Table 6.

4.3. Distribution of U and Th in Mercury and existence of an FeS layer

We developed a model to estimate the concentrations of heat-producing elements U and Th in the BSM for different plausible core

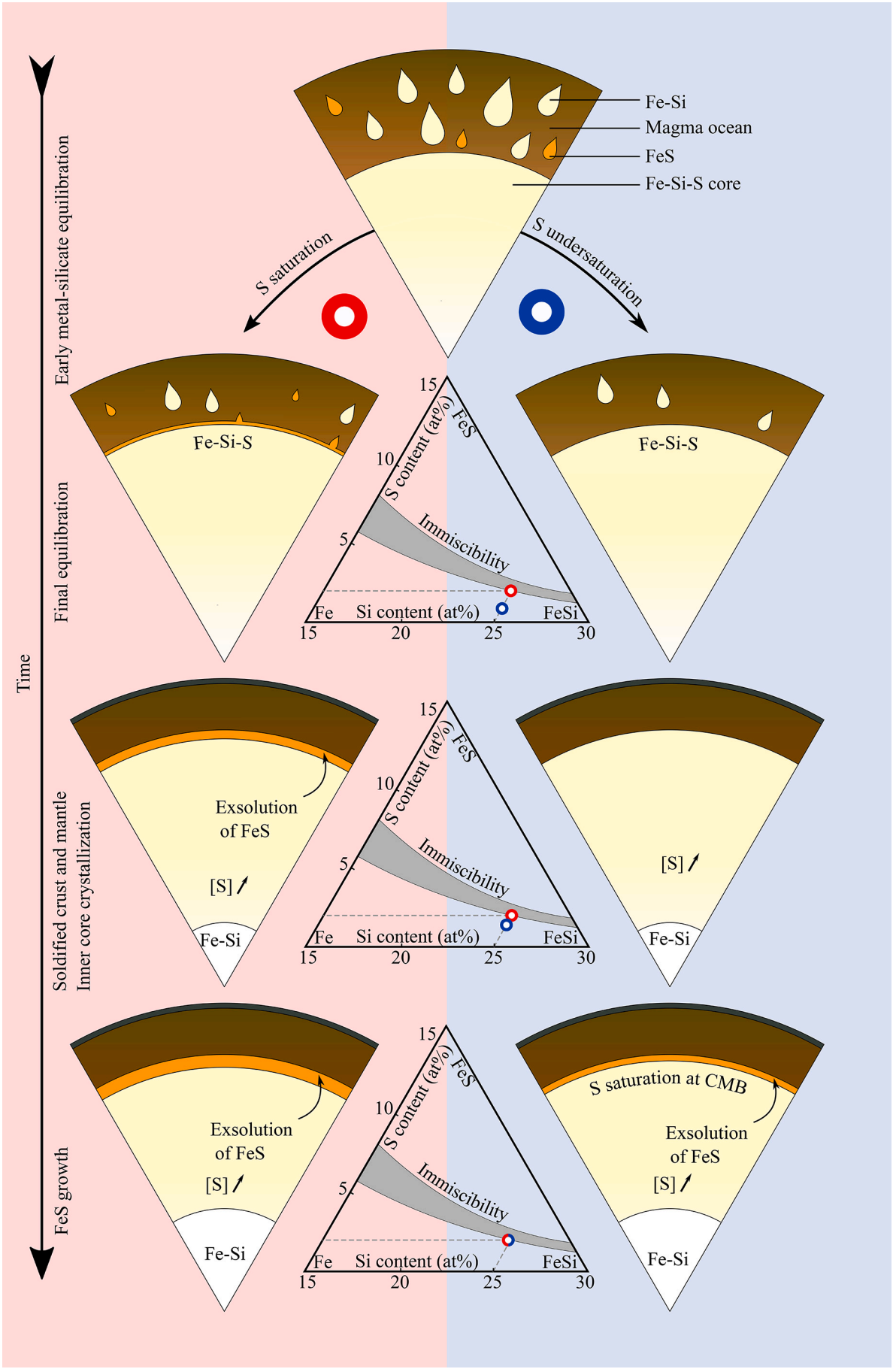

(caption on next page)

Fig. 7. Scenarios for the evolution of Mercury's interior during planetary cooling. Left panel, red background: the sulfide saturation scenario. Here, the excess of S in the mantle during differentiation results in the early formation of an FeS layer at the CMB. In this scenario, the formation of an Fe—Si inner core is possible, and also leads to the exsolution of FeS, further contributing to the formation of an FeS layer. The Fe-Si-S phase diagrams (modified after Morard and Katsura, 2010) shown in the middle indicate the hypothetical initial compositions of the liquid core for both scenarios (blue and red points corresponding to the two scenarios). Right panel, blue background: formation scenario of Mercury in case the BSM was undersaturated in S. Because sulfide is not initially saturated in the magma ocean, there is no early formation of an FeS layer. The crystallization of the Fe—Si inner core leads to the exsolution of FeS because the enrichment of S in the outer core drives the metal composition into the immiscibility field of the Fe-Si-S system. Based on Namur et al. (2016a), we considered the case where 2 at.% S was present in the metallic core.(For interpretation of the references to colour in this figure legend, the reader is referred to the web version of this article.)

and FeS layer formation scenarios (Fig. 7). In this model, we calculated the mass of each geochemical reservoir (metallic core, FeS layer, BSM) using their respective fixed densities and sizes (Hauck et al., 2013). We consider a fixed silicate layer thickness of 440 km and a maximum core radius of 2000 km, which decreases with increasing the thickness of the FeS layer from 0 to 100 km.

Two scenarios were considered for the differentiation of Mercury. In Scenario 1 (Fig. 7, left panel), Mercury is initially saturated in sulfide during primordial differentiation and FeS droplets form and sink in the magma ocean. Because they are less dense than Fe—Si metal, the FeS droplets aggregate to form an FeS layer at the core-mantle boundary in equilibrium with the magma ocean (Malavergne et al., 2014). In Scenario 2 (Fig. 7, right panel), Mercury is not initially saturated in sulfide, and the formation of an FeS layer (if present) results from the crystallization of the S-bearing Fe—Si core; the formation of an Fe—Si solid core results in increasing the S content of the outer residual liquid core, which exsolve FeS droplets when it exceeds the solubility of S at the pressure conditions of the CMB (Morard and Katsura, 2010; Charlier and Namur, 2019). This occurs after complete solidification of the magma ocean so that the FeS layer and the silicate portion do not equilibrate.

In both scenarios, we calculated the distribution of U and Th in the different reservoirs. The FeS/silicate partition coefficients for U and Th are calculated using Eq. (5). Oxygen fugacity was varied from IW − 7 to IW − 3. This redox range is relevant to the estimated fO_2 during differentiation (McCubbin et al., 2012) and corresponds to the range in the experiments used to parameterize the partition coefficients. Because it was not possible to precisely parameterize $D_U^{metal/silicate}$ and $D_{Th}^{metal/silicate}$ as a function of fO_2, we considered two end-member cases for metal-silicate partition coefficients, consisting in some of the highest and the lowest values of $D_U^{metal/silicate}$ found in our experiments and the literature between IW − 7 and IW − 3. $D_{Th}^{metal/silicate}$ was then calculated using Eq. (7). The first case corresponds to a high incorporation of U and Th in the core ($D_U^{metal/silicate} = 0.01$ and $D_{Th}^{metal/silicate} = 0.0018$), and the second case to a low incorporation of these elements in the core ($D_U^{metal/silicate} = 0.0001$ and $D_{Th}^{metal/silicate} = 0.00009$).

To model an initially sulfide-saturated Mercury (Scenario 1; Fig. 7, left panel), we considered that the three geochemical reservoirs (BSM, FeS layer, and core) were in equilibrium during Mercury's primordial differentiation. U, and to a lesser extent, Th can be slightly incorporated into the core. This incorporation slightly fractionates U and Th, so that the bulk silicate Th/U slightly increases. The fractionation is negligible in the case where $D_U^{metal/silicate}$ is low (< 0.001). While Th is mostly lithophile, U is strongly incorporated into FeS at low fO_2 conditions (<IW − 5), with $D_U^{FeS/silicate} \sim 1$ at IW − 6. Under the least reduced conditions, however, U mainly dominantly stays in the BSM along with Th. It means that although almost no fractionation occurs between these elements above IW − 5, they are increasingly fractionated under increasingly reducing conditions if an FeS layer is present. As the thickness of the FeS layer increases, this fractionation becomes larger because FeS incorporates large amounts of U and lower amounts of Th, as observed in Boujibar et al. (2019). Therefore, the amount of U in the BSM, and thus, its Th/U ratio, depend on the thickness of the

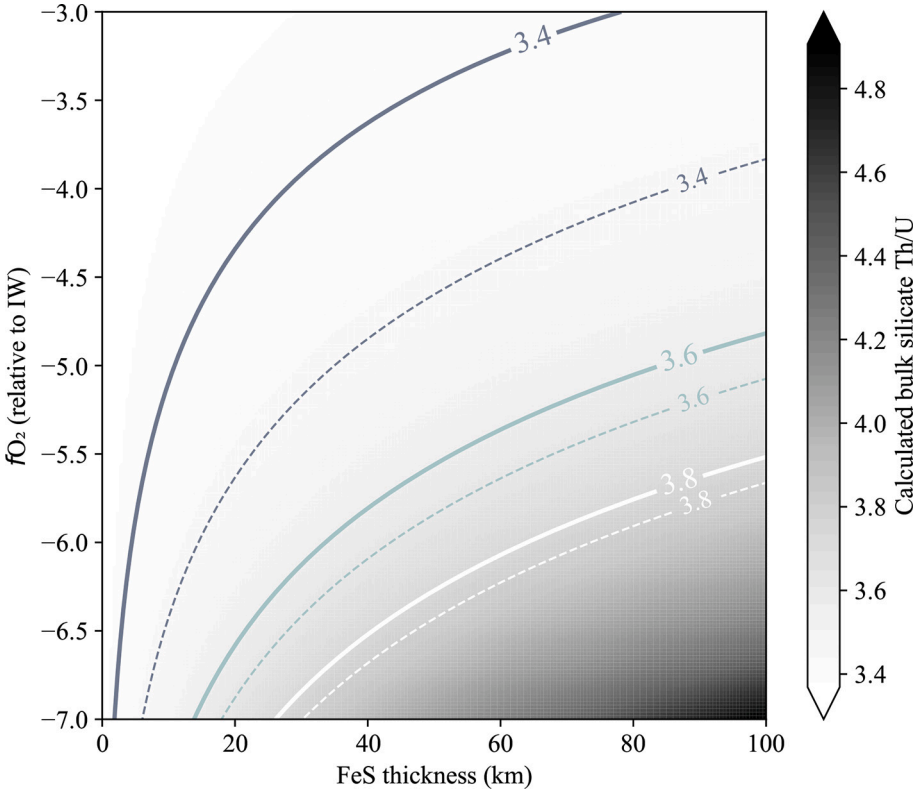

Fig. 8. The calculated Th/U ratio of the BSM as a function of the FeS layer thickness and oxygen fugacity during primordial differentiation. The mesh and the thick lines were calculated with high incorporation of U and Th in the core, and the dashed lines were calculated with low incorporation of U and Th in the core. The initial Th/U ratio in this model is taken as 3.3, the average in EH chondrites. MESSENGER measured surface Th/U ratios of 2.5 ± 0.9; therefore, any value above 3.4 is unlikely.

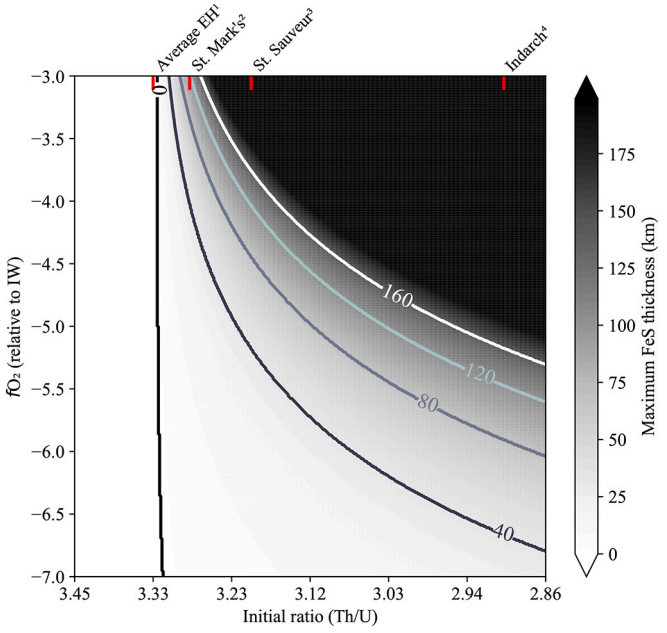

Fig. 9. Maximum thickness of an FeS layer formed in equilibrium with the core and the BSM as a function of oxygen fugacity and the initial Th/U ratio. The mesh and the lines were calculated with high incorporation of U and Th in the core. The low incorporation model slightly offsets all the lines to the left, but its effect is not significant. The maximum FeS layer thickness represents the point where the remaining silicate Th/U ratio is equal to the upper value measured at the surface (~3.4), so that it is impossible to have a thicker FeS layer without increasing the Th/U ratio above 3.4. The black part in the upper right part of the plot represents thicknesses >200 km. The Th/U ratios of some enstatite chondrites (EH), as well as their global average value, are shown at the top. 1: Wasson and Kallemeyn (1988); 2: Barrat et al. (2014); 3,4: Dauphas and Pourmand (2011).

hypothetical FeS layer and the oxygen fugacity during differentiation.

In contrast, if Mercury was not initially sulfide-saturated, the FeS layer formed via the exsolution of FeS from the liquid core because of crystallization of Fe—Si solids (Miozzi et al., 2022; Edmund et al., 2022; Scenario 2; Fig. 7, right panel). In this case, most of U and Th remain in the BSM during early differentiation, and only a small amount of U is incorporated into the core. If the inner core crystallized to exsolve FeS, it is probable that this process occurred after the solidification of the BSM (i.e., after mantle/crust differentiation) and the FeS layer would only be in equilibrium with the liquid core, i.e., it would not reequilibrate with the solidified mantle. Formation of the FeS layer would thus deplete the core in U and Th because these elements have a stronger affinity for FeS than for metal under reducing conditions. Ultimately, in this scenario, the planet should have a silicate Th/U ratio similar to the chondritic ratio, and heat-producing elements should be concentrated in the BSM. This exsolution of FeS from the liquid core could also happen in the first scenario, which would increase the size of the FeS layer and change its composition, but would ultimately not change the composition of the already solidified silicate part (Scenario 1; Fig. 7, left panel).

The calculated Th/U ratios of the two scenarios can be compared with Th and U measurements at the surface of Mercury by *MESSENGER*. We assume that U and Th were not fractionated during partial melting of the mantle and formation of the crust. This assumption is reasonable because, on Earth, these elements are highly incompatible and do not fractionate during partial melting (Wipperfurth et al., 2018). However, because the BSM likely hosts sulfides such as CaS or MgS, this assumption may not be fully correct, as discussed below (Section 4.5). Chemical data from *MESSENGER* provided surface Th/U ratios of 2.5 ± 0.9, so that the upper limit for surface Th/U is 3.4 for 1σ. If Mercury initially had the same Th/U ratio as the average EH chondritic ratio (3.3, Javoy and Kaminski, 2014), the fractionation of U and Th during the formation of even a thin (<20 km) FeS layer under reducing conditions during the primordial differentiation of the planet (Scenario 1; Fig. 7, left panel) would increase the BSM Th/U ratio above the upper limit of 3.4 (Fig. 8), unless the planet formed at fO_2 conditons above IW − 4 (Fig. 8). If incorporation of U and Th in the core is low (dashed lines), it is possible to form a thicker FeS layer (up to 80 km) at high fO_2 (<IW-4), but we do not observe significant changes between high and low incorporation of U and Th into the core for more reducing conditions, meaning that it is the formation of a FeS layer that dominates U—Th fractionation at these fO_2.

To reconcile the observed Th/U ratios with the existence of a thick FeS layer, the bulk planet could have an initial Th/U ratio lower than 3.3. Indeed, enstatite chondrites have Th/U values as low as ~2.7 and up to >4 (Javoy and Kaminski, 2014 and references therein). However, only a few meteorites exhibit low Th/U, and there are still large uncertainties between different studies; for exemple, Barrat et al. (2014) found a ratio of 3.84 in Indarch, while Dauphas and Pourmand (2011) and Morgan and Lovering (1968) found a value of 2.9 and 2.66 respectively. Therefore, we calculated the maximum FeS layer thickness that would lead to a surface Th/U ratio < 3.4 for a range of bulk Th/U ratios of 2.86–3.45 (Fig. 9).

As shown in Fig. 9, fO_2 conditions >IW-4 allow the existence of a thick FeS layer at any bulk initial Th/U because low fractionation at these conditions only slightly affects the resulting silicate Th/U ratio. However, at lower fO_2 (<IW-5) it is only possible to reconcile the presence of an FeS layer with lower bulk initial Th/U than the average observed in EH (3.3); if the bulk Th/U is as low as 2.9, it is possible to have an FeS layer up to 80 km thick at IW-6. As 3.4 is the upper limit of the measured ratio on the surface of Mercury (Peplowski et al., 2011), it is probable that the initial ratio was lower than the average value of 3.3 for EH meteorites. However, as a Th/U ratio below 3 is rarely observed in chondrites, it is plausible that the surface ratio of 2.5 ± 0.9 is the combined result of a low initial ratio and the absence of an FeS layer formed under reducing conditions in equilibrium with the magma ocean. Indeeed, even if the initial ratio was around ~2.7, the lowest observed in chondrites (Morgan and Lovering, 1968), the presence an FeS layer would increase the surface ratio to values close to the upper limit.

In summary, the presence of an FeS layer formed under reducing conditions in equilibrium with the silicate melt contradicts the data from *MESSENGER* (which measured a slightly sub-chondritic Th/U ratio) if the bulk Th/U was similar to the mean value found in enstatite chondrites. If the surface Th/U ratio is close to the maximum measured by MESSENGER (3.4; 2.5 ± 0.9, Peplowski et al., 2011), it is nevertheless possible to form an FeS layer if: 1) the planet formed under less reduced conditions (>IW − 4), because U partitions only slightly into FeS, which does not significantly affect the resulting silicate Th/U ratio and/or 2) the initial Th/U ratio was at the lower end of chondritic data. These outcomes indicate that, except if the initial Th/U was sub-chondritic and that Mercury formed an FeS layer under reducing conditions, almost all of Mercury's initial U and Th contents should reside in the BSM. If the planet formed under very reducing conditions without an FeS layer, there is no other reservoir to incorporate large amounts of U and Th. Alternatively, if Mercury formed under more oxidized conditions and hosts an FeS layer, then U and Th did not partition into the FeS layer.

Our model can be used to calculate the absolute concentrations of U and Th in the BSM, assuming that Mercury formed from material with chondritic concentration. Our calculations indicate that in the case of initial sulfide saturation, the U concentration in the BSM depends mainly on the thickness of the FeS layer, as well as the oxygen fugacity during formation. We considered that bulk Mercury contains 9 ppb U (the average concentration in EH chondrites; Javoy and Kaminski, 2014) and calculated the BSM U concentration to be ~35 ppb in the absence of an FeS layer (Fig. 10, upper panel). If the layer formed in equilibrium with the BSM, the BSM U concentration is ~33 ppb at the least reducing

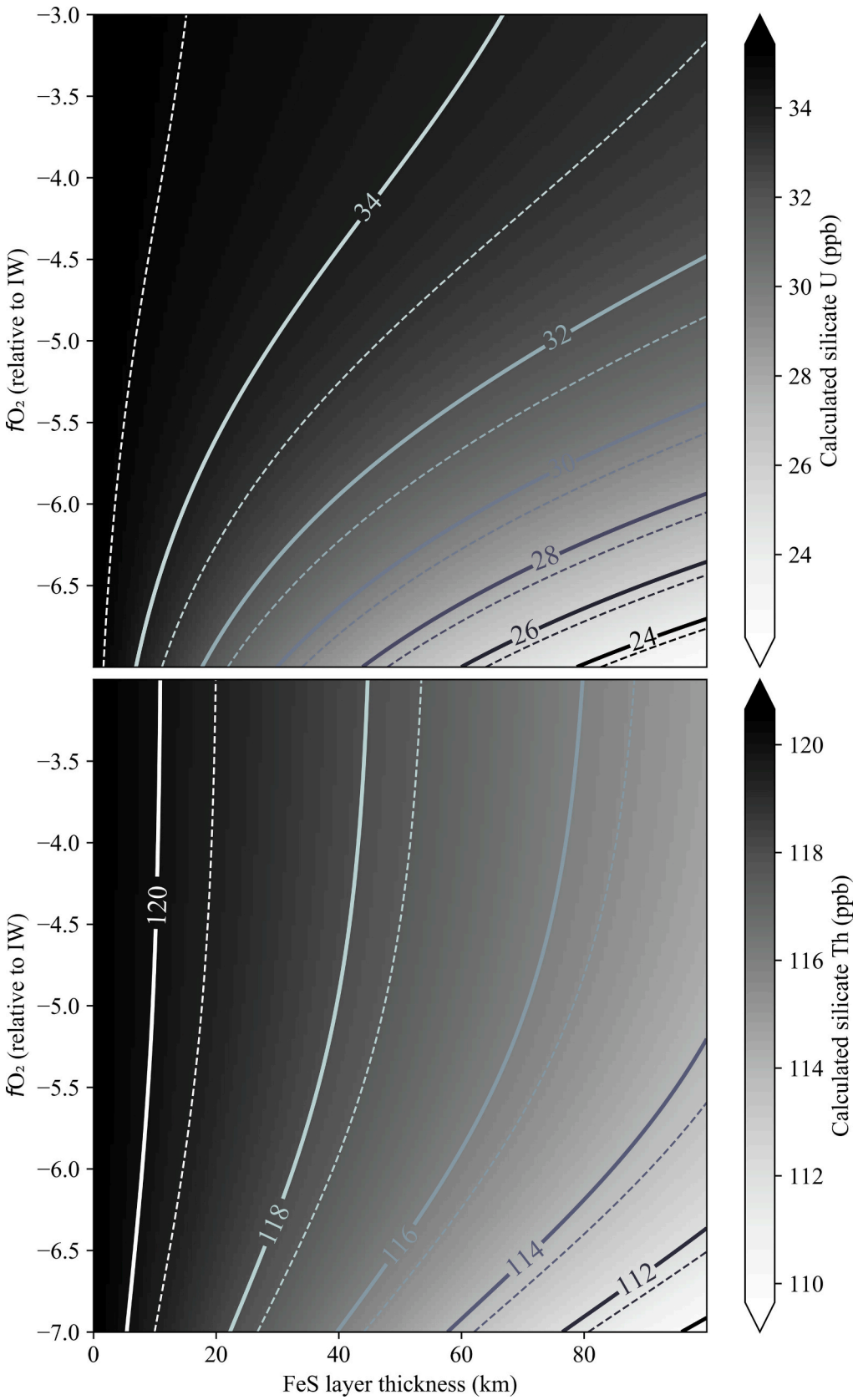

Fig. 10. U (upper) and Th (lower) concentrations (ppb) in the BSM as a function of fO_2 and the thickness of the FeS layer (in km). The mesh and the thick lines were calculated with high incorporation of U and Th in the core, and the dashed lines were calculated with low incorporation of U and Th in the core. Thick lines and dahsed lines of the same colour have the same value. The content of U in silicate part is relatively more affected by the presence of a thick FeS layer formed at low fO_2 than Th.

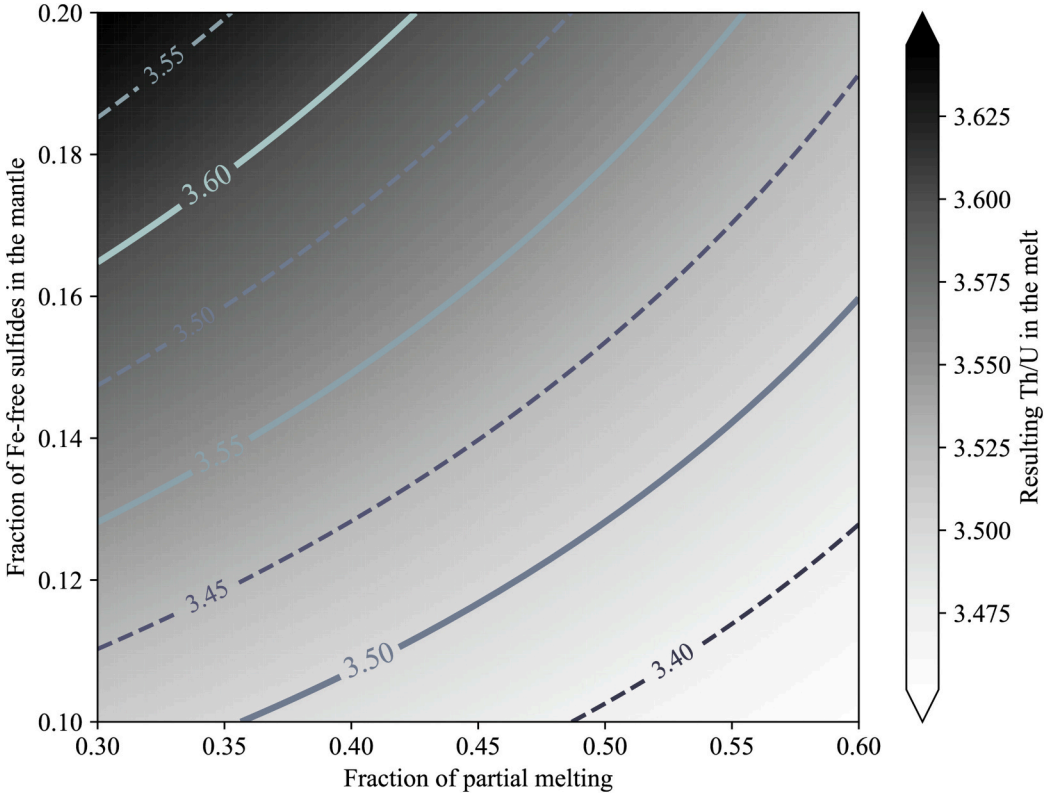

Fig. 11. The influence of residual Fe-free sulfides in the mantle and the degree of partial melting on the surface Th/U ratio. The presence of Fe-free sulfides slightly increases the surface Th/U ratio, especially at relatively low degrees of partial melting. In this figure, $fO2$ during differentiation was fixed at IW − 5 (Namur et al., 2016a) to isolate the effects of sulfides in the mantle and the degree of partial melting. We also consider that no FeS layer formed. The mesh and the thick lines were calculated with high incorporation of U and Th in the core, and the dashed lines were calculated with low incorporation of U and Th in the core. Although uncertainties remain on the exact values of $D^{sulfide/silicate}$ for U and Th in Fe-free sulfides, it seems that a fractionation of U and Th in the presence of mantle sulfides is possible.

oxygen fugacity conditions (IW − 3, 100-km thick FeS layer) to as low as ~23 ppb under the most reducing conditions (IW − 6, with a 100-km thick FeS layer) (Fig. 10, upper panel). Th is less impacted by the formation of the FeS layer and by fO_2 conditions than U, and for an initial bulk planetary concentration of 30 ppb (Javoy and Kaminski, 2014), we calculated the BSM Th concentration to be ~110 ppb for an FeS layer 100 km thick under the most reducing conditions or up to ~121 ppb in the absence of an FeS layer (Fig. 10, lower panel).

4.4. Sulfides in the mantle and their impact on U and Th

Under reducing conditions, sulfur solubility in silicate melts increases by up to several wt% compared to Earth like fO_2 conditions (Namur et al., 2016a). Because oxygen fugacity is very low in Mercury (IW − 7 to IW − 3; McCubbin et al., 2012), Mercury's magma ocean is thought to have contained abundant sulfur, which would have formed sulfides once the magma ocean reached sulfide saturation (Boukaré et al., 2019). These sulfides may have sunk or floated depending on their relative densities and that of the silicate magma ocean (Parman et al., 2016; Boukaré et al., 2019; Mouser et al., 2021). Cooling of the magma ocean would have decreased the SCSS, which is strongly temperature dependent (Namur et al., 2016a), continuously producing sulfides. In contrast, in an initially sulfide-undersaturated magma ocean, no sulfide would have been present during the early stages of silicate magma crystallization; i.e., the sulfur content of the magma ocean was below the SCSS. As silicate cumulates crystallized, the residual silicate liquid became progressively enriched in sulfur, and the crystallization of Fe-free sulfides (such as MgS) in the magma ocean began at a depth that depends on the initial S content of the magma ocean and fO_2. At fixed bulk S content, more reducing conditions (and thus, higher S solubility) would have resulted in a shallower depth of sulfides saturation (Boukaré et al., 2019). In our model, we consider the presence of sulfides during mantle partial melting to calculate the global partition coefficient between the residual mantle and the silicate melt that ultimately formed the crust of Mercury. The details of the modeling can be found in Appendix 1.

To model the effect of sulfides in the mantle on the silicate Th/U, we use the following parameters: fO_2 = IW − 7 to IW − 3, no FeS layer, abundance of residual MgS sulfides during partial melting from 10 to 20%, and 30–60% partial melting (Namur et al., 2016a, 2016b). Initial concentrations of U and Th in the building blocks were 9 and 30 ppb, respectively (Th/U = 3.3). Our modeling results show that the presence of Fe-free sulfides in the mantle during partial melting produces melts with higher Th/U ratios because the residual mantle sulfides fractionated U and Th. However, this fractionation effect is not significant, and is even less important at higher degrees of partial melting (Fig. 11). Our assumption that the bulk silicate Th/U ratio was equivalent to the surface ratio is thus somewhat challenged by the presence of mantle sulfides. As such, it would mean that even higher fO_2 conditions or even lower initial bulk Th/U are needed to have simultaneously mantle sulfides and an FeS layer to have a surface Th/U below 3.4. Namur et al. (2016a), showed that the presence of these sulfides are probable in the mantle, so that it makes the presence of an FeS layer even more unlikely.

By varying all the parameters over possible ranges (FeS thickness, 0–100 km; fO_2, IW-3 – IW-7; amount of Fe-free sulfides in the mantle, 10–20 wt%; and partial melting degree, 30–60%), our models suggest that after crust formation, lavas contain ~180–400 ppb Th and ~ 35–115 ppb U. These concentrations match those measured at the surface by *MESSENGER*: 220 ± 60 ppb Th and 90 ± 20 ppb U (Peplowski et al., 2011), except for the lowest calculated U concentrations, which result from the presence of a thick FeS layer (100 km) formed at the lowest fO_2 (IW-7) and for lavas formed from a very high degree of partial melting (60%). The abundance of these elements on the surface is largely affected by the degree of partial melting, as they are very

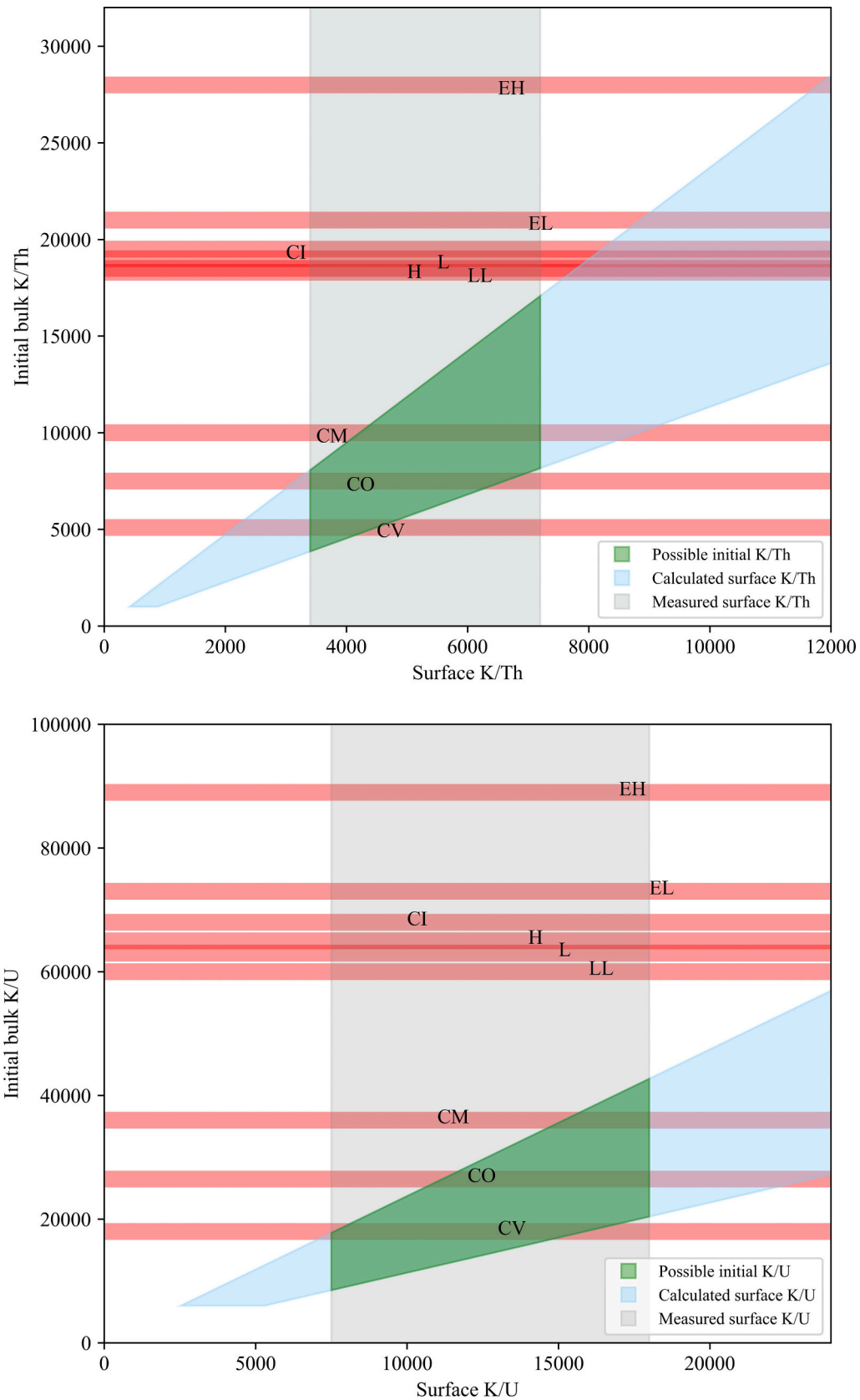

Fig. 12. The expected range of K/Th (top) and K/U (bottom) on Mercury's surface (blue shaded area) depending on the initial bulk planet's K/Th and K/U ratios, respectively. The gray area represents MESSENGER measurements of the K/Th and K/U ratios on the surface of Mercury. Horizontal red shaded areas represent the average K/Th and K/U ratios of different chondrites. EH and EL, enstatite chondrites; H, L, LL: ordinary chondrites; CI, CM, CO, CV: carbonaceous chondrites. Data for the chondritic ratios come from Wasson and Kallemeyn (1988). (For interpretation of the references to colour in this figure legend, the reader is referred to the web version of this article.)

incompatible. High partial melting (~60%) yields the lowest U and Th concentrations, and inversely. The presence of an FeS layer at low oxygen fugacity affects more strongly the surface concentration of U than Th, but this effect is modest compared to the effect of partial melting. The effect of mantle sulfides on the surface concentration of U and Th is significant, but not as important as the presence of an FeS layer. Finally, the U content measured on the surface corresponds in our model to scenarios where no FeS layer formed under reducing conditions.

4.5. The volatile inventory of Mercury

Both U and Th are refractory elements, whereas K is moderately volatile. Because these three elements behave incompatibly and are not fractionated during partial melting, the surficial K/Th and K/U ratios are powerful tools for understanding Mercury's volatile budget (Peplowski et al., 2011). The mean K/Th value of Mercury's surface (5200 ± 1800) is similar to that of the other inner planets (Peplowski et al., 2011), a surprising discovery because Mercury was thought to be volatile-depleted due to its proximity to the Sun (Albarède, 2009; McCubbin et al., 2012). Boujibar et al. (2019) predicted that a bulk K/U ratio in agreement with models of volatile depletion with heliocentric distance (Albarède, 2009), and a bulk K/Th similar to other terrestrial planets are consistent with the formation of a thick FeS layer under reducing conditions (IW-5.5). On the other hand, they also showed that higher oxygen fugacity conditions (IW-4) would lead to bulk K/Th and K/U ratios close to the ones measured on Mercury's surface regardless of the thickness of an FeS layer (Boujibar et al., 2019).

We determined the values of bulk K/Th and K/U ratios needed to match the values measured by MESSENGER. To do so, we used our differentiation model with bulk chondritic (EH) K/Th and K/U ratios of ~26,000 and ~ 90,000, respectively (Lodders and Fegley, 1998). In our model, we used high incorporation of U and Th into the core ($D_{Th}^{metal/silicate}$ of 0.01 and $D_{Th}^{metal/silicate}$ of 0.0018; Section 4.3), and we used Eq. (5) to calculate $D_{K}^{metal/silicate}$. At low oxygen fugacity (IW-5.5) and without an FeS layer, we obtained after differentiation and partial melting a surface K/Th and K/U of 18,000 ± 6000 and 57,000 ± 20,000, depending on the specific compatibilities of K and Th in silicate minerals (forsterite and enstatite, see Appendix 1) and the degree of partial melting. This is respectively 2–4 and 3–6 times higher than the K/Th and K/U ratios measured on the surface of Mercury. If we calculate the surface K/Th and K/U ratios using different initial K/Th and K/U values (and fixing the initial Th/U ratio, so that only the initial K content varies), we find that only K-depleted carbonaceous chondrites can account for the observed surface ratio (Fig. 12), contradicting hypotheses about the chemistry of Mercury's building blocks. It is more likely that, although the surface is relatively rich in volatile elements (S, K, and Na; Nittler et al., 2011; Peplowski et al., 2012, 2014), Mercury probably experienced a global loss of potassium. This volatile loss process could have been similar to the process that depleted the Earth and Mars in volatiles (i.e., early volatilization and/or a hidden reservoir of K; Humayun and Clayton, 1995; McDonough, 2016), but other potential causes remain, such as the vaporization of K from the surface by solar radiation (Dauphas et al., 2022 and references therein). Therefore, further work is needed to develop a model of Mercury's formation that can account for its sub-chondritic surface K/Th and K/U ratios and chondritic surface S content, knowing that S is more volatile than K.

5. Conclusions

We performed 20 experiments on materials representative of the bulk silicate portion of Mercury under very reducing conditions (IW-8.5 to IW-1.4), at 0.1–3 GPa, and 1520–1720 °C. The major, minor, and trace element concentrations of the different liquids (and solids for the experiment with MgS) present in the retrieved samples were measured to establish partition coefficients for >30 elements between silicate melt, metallic melt, sulfide melt (FeS), and MgS sulfides. We developed a mass-balance model for Mercury to evaluate the distribution of heat-producing elements (U and Th) in different reservoirs (BSM, mantle sulfides, the hypothetical FeS layer, and the core). This model was applied to two differentiation scenarios; in the first one, the FeS layer formed during differentiation from a S-saturated Mercury, while in equilibrium with both the silicate part and the core, while in the second scenario, the FeS layer formed from exsolution of an FeS-saturated core during its crystallization. We show that *MESSENGER* measurements of surface Th/U ratios preclude the existence of an FeS layer that formed under reduced conditions (< IW-4) in equilibrium with the BSM if Mercury's building blocks had mean chondritic Th/U (around 3.3). It is nonetheless possible to reconcile the presence of an FeS layer if conditions were more oxidizing during the differentiation (> IW-4) and/or if the initial Th/U ratio of Mercury was at the lower end of chondritic data (Th/U < 3). Our results show that sulfides in the Mercurian mantle, such as MgS, should not incorporate significant amounts of U and Th, but that their presence would contribute to increase the silicate Th/U ratio at the surface. Almost all of Mercury's U and Th should be stored in the BSM, independently of the differentiation scenario considered, except in the case of the formation of an FeS layer under reducing conditions from material with sub-chondritic Th/U. Regarding Mercury's volatile inventory, measured surface K/Th and K/U ratios are respectively 2–4 and 3–6 times lower than expected if the initial bulk ratios were similar to those of enstatite chondrites. Although it remains possible that Mercury formed from K-poor materials, it is likely that Mercury lost a large portion of its K in the early history, as did Earth. Processes that could reconcile this K-loss with the high surface concentrations of other volatile elements (S, Na) remain an open question for future studies.

Declaration of Competing Interest

The authors declare that they have no known competing financial interests or personal relationships that could have appeared to influence the work reported in this paper.

Data availability

Data will be made available on request.

Acknowledgements

HP was supported by the FRIA-FNRS (Fonds pour la Formation à la Recherche dans l'Industrie et dans l'Agriculture - Fonds de la Recherche Scientifique) (grant FC 31865). ON acknowledges support from FWO through an Odysseus grant. BC is a Research Associate of the Belgian Fund for Scientific Research-FNRS. C. McCammon is thanked for her help with piston cylinder experiments at BGI. O. Namur acknowledges support from the DFG Core Facility for High-Pressure Research from the German Science Foundation for the high-pressure experiments performed at BGI. We are grateful to Rob Dennen for editing carefully the manuscript. We thank Asmaa Boujibar and an anonymous reviewer for their comments that greatly improved the manuscript. Doris Breuer is acknowledged for handling the manuscript.

Appendix A. Supplementary data

Supplementary materials containing details on experimental conditions, EPMA data, LA-ICP-MS data, and partition coefficients for every experiment are available. Another file contains a comparison between the fO_2 calculated using Namur et al. (2016a) equation and using Si-SiO_2 equilibrium. Supplementary data to this article can be found online at https://doi.org/10.1016/j.icarus.2023.115699.

Appendix 1

To evaluate the fractionation of K/Th, K/U, and Th/U ratios caused by the magmatic processes responsible for the formation of Mercury's secondary crust, we modeled the evolution of U, Th, and K concentrations during mantle partial melting. We considered that the crustal lavas formed from a high degree of partial melting (20–50 vol%) of a peridotitic mantle (Charlier et al., 2013; Namur et al., 2016b; Namur and Charlier, 2017), and calculated the abundances of K, Th, and U in these lavas using Shaw's batch melting equation (Shaw, 1970):

$$\frac{C_L^M}{C_0^M} = \frac{1}{(D + (D-1)) \bullet F} \quad (1)$$

where C_L^M is the concentration of element M in the melt, C_0^M is the concentration of element M in the primordial mantle (corresponding to the BSM), D is the rock/melt partition coefficient of element M, and F is the melt fraction. Although this equation does not simulate the complex processes occurring in mantle plumes, we used it to evaluate the global impact of partial melting on the distributions of heat-producing elements between the mantle and the melts produced. The mantle residue in equilibrium with the lavas is composed of olivine (forsterite) and enstatite in unknown relative proportions (Namur et al., 2016b). The partitioning of K, U, and Th between these two minerals and mafic melts is not well constrained. Based on the partitioning data of Bédard (2005, 2007) and Cartier et al. (2014), we considered that reasonable ranges of $D^{mantle/melt}$ for Eq. (1) are: $D_K = 0.005–0.5$, $D_{Th} = 0.0005–0.1$, and $D_U = 0.0005–0.1$. Although the partitioning of these elements is not well defined, Th and U have almost identical electronic properties (Shannon, 1976) and are thus expected to behave similarly during magmatic processes. Moreover, crustal production on Earth does not fractionate U and Th (Wipperfurth et al., 2018) and there seems to be no fractionationation of Th and U in enstatites under highly reducing conditions (Cartier et al., 2014). For these reasons, we introduced two additional constraints:$0.5 < D_{Th}/D_U < 2$ and $0.1 < D_{Th}/D_K < 10$.

Using the data on U and Th partitioning into MgS from experiment Y087–2, we obtain $D_U^{MgS/silicate} \approx 0.5$ and $D_{Th}^{MgS/silicate} \approx 0.1$ at ~IW − 8.5. Because no other experimental D_U or D_{Th} values have been determined for MgS or CaS, we used the bracketing ranges of values $D_U^{sulfide/silicate} = 0.1–1$ and $D_{Th}^{sulfide/silicate} = 0.01–0.1$. We also considered $D_K^{sulfde/silicate} = 0.01–0.1$.

References

Albarède, F., 2009. Volatile accretion history of the terrestrial planets and dynamic implications. Nature 461, 1227–1233.

Anderson, J.D., Colombo, G., Esposito, P.B., Lau, E.L., Trager, G.B., 1987. The mass, gravity field, and ephemeris of Mercury. Icarus 71 (3), 337–349.

Anzures, B.A., Parman, S.W., Milliken, R.E., Namur, O., Cartier, C., Wang, S., 2020. Effect of sulfur speciation on chemical and physical properties of very reduced mercurian melts. Geochim. Cosmochim. Acta 286, 1–18.

Ash, M.E., Shapiro, I.I., Smith, W.B., 1971. The system of planetary masses: new results show that Pluto's mass cannot be determined reliably from existing data. Science 174 (4009), 551–556.

Barrat, J.A., Zanda, B., Jambon, A., Bollinger, C., 2014. The lithophile trace elements in enstatite chondrites. Geochim. Cosmochim. Acta 128, 71–94.

Bédard, J.H., 2005. Partitioning coefficients between olivine and silicate melts. Lithos 83, 394–419.

Bédard, J.H., 2007. Trace element partitioning coefficients between silicate melts and orthopyroxene: parameterizations of D variations. Chem. Geol. 244, 263–303.

Benkhoff, J., Van Casteren, J., Hayakawa, H., Fujimoto, M., Laakso, H., Novara, M., Ferri, P., Middleton, H.R., Ziethe, R., 2010. BepiColombo—comprehensive exploration of mercury: mission overview and science goals. Planet. Space Sci. 58 (1–2), 2–20.

Berndt, J., Liebske, C., Holtz, F., Freise, M., Nowak, M., Ziegenbein, D., Hurkuck, W., Koepke, J., 2002. A combined rapid-quench and H-2-membrane setup for internally heated pressure vessels: description and application for water solubility in basaltic melts. Am. Mineral. 87, 1717–1726.

Berthet, S., Malavergne, V., Righter, K., 2009. Melting of the Indarch meteorite (EH4 chondrite) at 1 GPa and variable oxygen fugacity: implications for early planetary differentiation processes. Geochim. Cosmochim. Acta 73 (20), 6402–6420.

Bouhifd, M.A., Gautron, L., Bolfan-Casanova, N., Malavergne, V., Hammouda, T., Andrault, D., Jephcoat, A.P., 2007. Potassium partitioning into molten iron alloys at high-pressure: implications for Earth's core. Phys. Earth Planet. Inter. 160 (1), 22–33.

Bouhifd, M.A., Andrault, D., Bolfan-Casanova, N., Hammouda, T., Devidal, J.-L., 2013. Metal-silicate partitioning of Pb and U: effects of metal composition and oxygen fugacity. Geochim. Cosmochim. Acta 114, 13–28.

Boujibar, A., Andrault, D., Bouhifd, M.A., Bolfan-Casanova, N., Devidal, J.L., Trcera, N., 2014. Metal–silicate partitioning of sulphur, new experimental and thermodynamic constraints on planetary accretion. Earth Planet. Sci. Lett. 391, 42–54.

Boujibar, A., Habermann, M., Righter, K., Ross, D.K., Pando, K., Righter, M., Chidester, B. A., Danielson, L.R., 2019. U, Th, and K partitioning between metal, silicate, and sulfide and implications for Mercury's structure, volatile content, and radioactive heat production. Am. Mineral. 104, 1221–1237.

Boukaré, C.E., Parman, S.W., Parmentier, E.M., Anzures, B.A., 2019. Production and preservation of sulfide layering in Mercury's mantle. J. Geophys. Res. Planets 124, 3354–3372.

Bunce, E.J., Martindale, A., Lindsay, S., Muinonen, K., Rothery, D.A., Pearson, J., McDonnell, I., Thomas, C., Thornhill, J., Tikkanen, T., Feldman, C., Huovelin, J., Korpela, S., Esko, E., Lehtolainen, A., Treis, J., Majewski, P., Hilchenbach, M., Väisänen, T., Luttinen, A., Kohout, T., Penttilä, A., Bridges, J., Joy, K.H., Alcacera-Gil, M.A., Alibert, G., Anand, M., Bannister, N., Barcelo-Garcia, C., Bicknell, C., Blake, O., Bland, P., Butcher, G., Cheney, A., Christensen, U., Crawford, T., Crawford, I.A., Dennerl, K., Dougherty, M., Drumm, P., Fairbend, R., Genzer, M., Grande, M., Hall, G.P., Hodnett, R., Houghton, P., Imber, S., Kallio, E., Lara, M.L., Balado Margeli, A., Mas-Hesse, M.J., Maurice, S., Milan, S., Millington-Hotze, P., Nenonen, S., Nittler, L., Okada, T., Ormö, J., Perez-Mercader, J., Poyner, R., Robert, E., Ross, D., Pajas-Sanz, M., Schyns, E., Seguy, J., Strüder, L., Vaudon, N., Viceira-Martín, J., Williams, H., Willingale, D., Yeoman, T., 2020. The BepiColombo mercury imaging X-ray spectrometer: science goals, instrument performance and operations. Space Sci. Rev. 216, 1–38.

Cartier, C., 2014. Comportement des terres rares (REE) et des éléments fortement chargés (HSFE) pendant la différenciation précoce de la Terre sous faible fugacité d'oxygène. Sciences de la Terre. Université Blaise Pascal - Clermont-Ferrand II.

Cartier, C., Wood, B.J., 2019. The role of reducing conditions in building Mercury. Elements 15, 39–45.

Cartier, C., Hammouda, T., Doucelance, R., Boyet, M., Devidal, J.-L., Moine, B., 2014. Experimental study of trace element partitioning between enstatite and melt in enstatite chondrites at low oxygen fugacities and 5 GPa. Geochim. Cosmochim. Acta 130, 167–187.

Cartier, C., Namur, O., Nittler, L.R., Weider, S.Z., Crapster-Pregont, E., Vorburger, A., Frank, E.A., Charlier, B., 2020. No FeS layer in Mercury? Evidence from Ti/Al measured by MESSENGER. Earth Planet. Sci. Lett. 534, 116108.

Chabot, N.L., Drake, M.J., 1999. Potassium solubility in metal: the effects of composition at 15 kbar and 1900 C on partitioning between iron alloys and silicate melts. Earth Planet. Sci. Lett. 172 (3–4), 323–335.

Chabot, N.L., Wollack, E.A., Klima, R.L., Minitti, M.E., 2014. Experimental constraints on Mercury's core composition. Earth Planet. Sci. Lett. 390, 199–208.

Charlier, B., Namur, O., 2019. The origin and differentiation of planet Mercury. Elem. Int. Mag. Miner. Geochem. Petrol. 15 (1), 9–14.

Charlier, B., Grove, T.L., Zuber, M.T., 2013. Phase equilibria of ultramafic compositions on Mercury and the origin of the compositional dichotomy. Earth Planet. Sci. Lett. 363, 50–60.

Chen, B., Li, J., Hauck, S.A., 2008. Non-ideal liquidus curve in the Fe-S system and Mercury's snowing core. Geophys. Res. Lett. 35 (7).

Condamine, P., Tournier, S., Charlier, B., Médard, E., Triantafyllou, A., Dalou, C., Tissandier, L., Lequin, D., Cartier, C., Füri, E., Burnard, P.G., Demouchy, S., Marrocchi, Y., 2022. Influence of intensive parameters and assemblies on friction

evolution during piston-cylinder experiments. Am. Mineral. J. Earth Planet. Mater. 107 (8), 1575–1581.
Corgne, A., Keshav, S., Fei, Y., McDonough, W.F., 2007. How much potassium is in the Earth's core? New insights from partitioning experiments. Earth Planet. Sci. Lett. 256, 567–576.
Corgne, A., Keshav, S., Wood, B.J., McDonough, W.F., Fei, Y., 2008. Metal–silicate partitioning and constraints on core composition and oxygen fugacity during Earth accretion. Geochim. Cosmochim. Acta 72 (2), 574–589.
Crozaz, G., Lundberg, L.L., 1995. The origin of oldhamite in unequilibrated enstatite chondrites. Geochim. Cosmochim. Acta 59, 3817–3831.
Dauphas, N., Pourmand, A., 2011. Hf–W–Th evidence for rapid growth of Mars and its status as a planetary embryo. Nature 473 (7348), 489–492.
Dauphas, N., Nie, N.X., Blanchard, M., Zhang, Z.J., Zeng, H., Hu, J.Y., Meheut, M., Visscher, C., Canup, R., Hopp, T., 2022. The extent, nature, and origin of K and Rb depletions and isotopic fractionations in earth, the moon, and other planetary bodies. Planet. Sci. J. 3 (2), 29.
Dickinson, T.L., Lofgren, G.E., McKay, G.A., 1990. REE partitioning between silicate liquid and immiscible sulfide liquid: the origin of the negative Eu anomaly in aubrite sulfides. In: Lunar and Planetary Science Conference XXI, p. 284.
Edmund, E., Morard, G., Baron, M.A., Rivoldini, A., Yokoo, S., Boccato, S., Hirose, K., Pakhomova, A., Antonangeli, D., 2022. The Fe-FeSi phase diagram at Mercury's core conditions. Nat. Commun. 13 (1), 387.
Evans, L.G., Peplowski, P.N., Rhodes, E.A., Lawrence, D.J., McCoy, T.J., Nittler, L.R., Solomon, S.C., Sprague, A.L., Stockstill-Cahill, K.R., Starr, R.D., Weider, S.Z., Boynton, W.V., Hamara, D.K., Goldsten, J.O., 2012. Major-element abundances on the surface of mercury: results from the MESSENGER gamma-ray spectrometer. J. Geophys. Res. Planets 117 (E12).
Evans, L.G., Peplowski, P.N., McCubbin, F.M., McCoy, T.J., Nittler, L.R., Zolotov, M.Y., Ebel, D.S., Lawrence, D.J., Starr, R.D., Weider, S.Z., Solomon, S.C., 2015. Chlorine on the surface of Mercury: MESSENGER gamma-ray measurements and implications for the planet's formation and evolution. Icarus 257, 417–427.
Genova, A., Goossens, S., Mazarico, E., Lemoine, F.G., Neumann, G.A., Kuang, W., Sabaka, T.J., Hauck, S.A., Smith, D.E., Solomon, S.C., Zuber, M.T., 2019. Geodetic evidence that Mercury has a solid inner core. Geophys. Res. Lett. 46 (7), 3625–3633.
Goossens, S., Renaud, J.P., Henning, W.G., Mazarico, E., Bertone, S., Genova, A., 2022. Evaluation of recent measurements of Mercury's moments of inertia and tides using a comprehensive Markov chain Monte Carlo method. Planet. Sci. J. 3 (2), 37.
Griffin, W.L., Powell, W.J., Pearson, N.J., O'Reilly, S.Y., 2008. GLITTER: data reduction software for laser ablation ICP-MS. In: Sylvester, P. (Ed.), Laser Ablation ICP-MS in the Earth Sciences: Current Practices and Outstanding Issues, Mineralogical Association of Canada. Short Course Series, 40, pp. 308–311.
Hammouda, T., Boyet, M., Frossard, P., Cartier, C., 2022. The message of oldhamites from enstatite chondrites. Prog. Earth Planet. Sci. 9 (1), 1–19.
Hauck, S.A., Margot, J.-L., Solomon, S.C., Phillips, R.J., Johnson, C.L., Lemoine, F.G., Mazarico, E., McCoy, T.J., Padovan, S., Peale, S.J., Perry, M.E., Smith, D.E., Zuber, M.T., 2013. The curious case of Mercury's internal structure. J. Geophys. Res. Planets 118, 1204–1220.
Howard, H.T., Tyler, G.L., Esposito, P.B., Anderson, J.D., Reasenberg, R.D., Shapiro, I.I., Fjeldbo, G., Kliore, A.J., Levy, G.S., Brunn, D.L., Dickinson, R., Edelson, R.E., Martin, W.L., Postal, R.B., Seidel, B., Sesplaukis, T.T., Shirley, D.L., Stelzried, C.T., Sweetnam, D.N., Wood, G.E., Zygielbaum, A.I., 1974. Mercury: results on mass, radius, ionosphere, and atmosphere from mariner 10 dual–frequency radio signals. Science 185, 179–180.
Humayun, M., Clayton, R.N., 1995. Potassium isotope cosmochemistry: genetic implications of volatile element depletion. Geochim. Cosmochim. Acta 59 (10), 2131–2148.
Ingrao, N.J., Hammouda, T., Boyet, M., Gaborieau, M., Moine, B.N., Vlastelic, I., Bouhifd, M.A., Devidal, J.L., Mathon, O., Testemale, D., Hazemann, J.L., Proux, O., 2019. Rare earth element partitioning between sulphides and melt: evidence for Yb^{2+} and Sm^{2+} in EH chondrites. Geochim. Cosmochim. Acta 265, 182–197.
Jantzen, T., Hack, K., Yazhenskikh, E., Müller, M., 2017. Evaluation of thermodynamic data and phase equilibria in the system Ca–Cr–Cu–Fe–Mg–Mn–S part I: binary and quasi-binary subsystems. Calphad 56, 270–285.
Javoy, M., Kaminski, E., 2014. Earth's Uranium and Thorium content and geoneutrinos fluxes based on enstatite chondrites. Earth Planet. Sci. Lett. 407, 1–8.
Kilburn, M.R., Wood, B.J., 1997. Metal–silicate partitioning and the incompatibility of S and Si during core formation. Earth Planet. Sci. Lett. 152, 139–148.
Kiseeva, E.S., Wood, B.J., 2013. A simple model for chalcophile element partitioning between sulphide and silicate liquids with geochemical applications. Earth Planet. Sci. Lett. 383, 68–81.
Kiseeva, E.S., Wood, B.J., 2015. The effects of composition and temperature on chalcophile and lithophile element partitioning into magmatic sulphides. Earth Planet. Sci. Lett. 424, 280–294.
Knibbe, J.S., van Westrenen, W., 2015. The interior configuration of planet Mercury constrained by moment of inertia and planetary contraction. J. Geophys. Res. Planets 120, 1904–1923.
Knibbe, J.S., van Westrenen, W., 2018. The thermal evolution of Mercury's Fe–Si core. Earth Planet. Sci. Lett. 482, 147–159.
Knibbe, J.S., Rivoldini, A., Luginbuhl, S.M., Namur, O., Charlier, B., Mezouar, M., Sifre, D., Berndt, J., Kono, Y., Neuville, D.R., van Westrenen, W., Van Hoolst, T., 2021. Mercury's interior structure constrained by density and P-wave velocity measurements of liquid Fe-Si-C alloys. J. Geophys. Res. Planets 126 (1) e2020JE006651.
Lehner, S.W., Petaev, M.I., Zolotov, M.Y., Buseck, P.R., 2013. Formation of niningerite by silicate sulfidation in EH3 enstatite chondrites. Geochim. Cosmochim. Acta 101, 34–56.
Lodders, K., Fegley, B., 1998. The Planetary scientist's Companion. Oxford University Press on Demand.
Malavergne, V., Tarrida, M., Combes, R., Bureau, H., Jones, J., Schwandt, C., 2007. New high-pressure and high-temperature metal/silicate partitioning of U and Pb: implications for the cores of the Earth and Mars. Geochim. Cosmochim. Acta 71, 2637–2655.
Malavergne, V., Toplis, M.J., Berthet, S., Jones, J., 2010. Highly reducing conditions during core formation on Mercury: implications for internal structure and the origin of a magnetic field. Icarus 206, 199–209.
Malavergne, V., Cordier, P., Righter, K., Brunet, F., Zanda, B., Addad, A., Smith, T., Bureau, H., Surblé, S., Raepsaet, C., Charon, E., Hewins, R.H., 2014. How Mercury can be the most reduced terrestrial planet and still store iron in its mantle. Earth Planet. Sci. Lett. 394, 186–197.
Margot, J.L., Peale, S.J., Jurgens, R.F., Slade, M.A., Holin, I.V., 2007. Large longitude libration of Mercury reveals a molten core. Science 316 (5825), 710–714.
Margot, J.L., Hauck, S.A.I., Mazarico, E., Padovan, S., Peale, S.J., 2018. Mercury's internal structure. In: Solomon, S.C., Nittler, L.R., Anderson, B.J. (Eds.), Mercury: The View after MESSENGER. Cambridge University Press, pp. 85–113.
McCoy, T.J., Dickinson, T.L., Lofgren, G.E., 1999. Partial melting of the Indarch (EH4) meteorite: a textural, chemical, and phase relations view of melting and melt migration. Meteorit. Planet. Sci. 34, 735–746.
McCubbin, F.M., Riner, M.A., Vander Kaaden, K.E., Burkemper, L.K., 2012. Is Mercury a volatile-rich planet? Geophys. Res. Lett. 39 (9).
McCubbin, F.M., Vander Kaaden, K.E., Peplowski, P.N., Bell, A.S., Nittler, L.R., Boyce, J. W., Evans, L.G., Keller, L.P., Elardo, S.M., McCoy, T.J., 2017. A low O/Si ratio on the surface of Mercury: evidence for silicon smelting? J. Geophys. Res. Planets 122, 2053–2076.
McDonough, W.F., 2016. The composition of the lower mantle and core. In: Deep Earth: Physics and Chemistry of the Lower Mantle and Core, pp. 143–159.
McLennan, S.M., 2003. Large-ion lithophile element fractionation during the early differentiation of Mars and the composition of the martian primitive mantle. Meteorit. Planet. Sci. 38, 895–904.
Mills, N.M., Agee, C.B., Draper, D.S., 2007. Metal-silicate partitioning of cesium: implications for core formation. Geochim. Cosmochim. Acta 71, 4066–4081.
Miozzi, F., Morard, G., Antonangeli, D., Baron, M.A., Pakhomova, A., Clark, A.N., Mezouar, M., Fiquet, G., 2022. The Fe-Si-C system at extreme P-T conditions: a possible core crystallization pathway for reduced planets. Geochim. Cosmochim. Acta 322, 129–142.
Morard, G., Katsura, T., 2010. Pressure–temperature cartography of Fe–S–Si immiscible system. Geochim. Cosmochim. Acta 74, 3659–3667.
Morgan, J.W., Lovering, J.F., 1968. Uranium and thorium abundances in chondritic meteorites. Talanta 15 (11), 1079–1095.
Mouser, M.D., Dygert, N., Anzures, B.A., Grambling, N.L., Hrubiak, R., Kono, Y., Shen, G., Parman, S.W., 2021. Experimental investigation of Mercury's magma ocean viscosity: implications for the formation of Mercury's cumulate mantle, its subsequent dynamic evolution, and crustal petrogenesis. J. Geophys. Res. Planets 126 (11) e2021JE006946.
Namur, O., Charlier, B., 2017. Silicate mineralogy at the surface of Mercury. Nat. Geosci. 10 (1), 9–13.
Namur, O., Charlier, B., Holtz, F., Cartier, C., McCammon, C., 2016a. Sulfur solubility in reduced mafic silicate melts: implications for the speciation and distribution of sulfur on Mercury. Earth Planet. Sci. Lett. 448, 102–114.
Namur, O., Collinet, M., Charlier, B., Grove, T.L., Holtz, F., McCammon, C., 2016b. Melting processes and mantle sources of lavas on Mercury. Earth Planet. Sci. Lett. 439, 117–128.
Nittler, L.R., Starr, R.D., Weider, S.Z., McCoy, T.J., Boynton, W.V., Ebel, D.S., Ernst, C.M., Evans, L.G., Goldsten, J.O., Hamara, D.K., Lawrence, D.J., McNutt, R.L., Schlemm, C. E., Solomon, S.C., Sprague, A.L., 2011. The major-element composition of Mercury's surface from MESSENGER x-ray spectrometry. Science 333, 1847–1850.
Nittler, L.R., Chabot, N.L., Grove, T.L., Peplowski, P.N., 2018a. The chemical composition of Mercury. In: Anderson, B.J., Nittler, L.R., Solomon, S.C. (Eds.), Mercury: The View after MESSENGER. Cambridge University Press, Cambridge, pp. 30–51.
Nittler, L.R., Boujibar, A., Crapster-Pregont, E., Frank, E.A., McCoy, T.J., McCubbin, F. M., Starr, R.D., Vander Kaaden, K.E., Vorburger, A., Weider, S.Z., 2018b. Heterogeneous distribution of chromium on Mercury. Mercury Curr. Future Sci. Innermost Planet 2047, 6095.
Parman, S.W., Parmentier, E.M., Wang, S., 2016, March. Crystallization of mercury's sulfur-rich magma ocean. In: 47th Annual Lunar and Planetary Science Conference (No. 1903, p. 2990).
Peplowski, P.N., Evans, L.G., Hauck, S.A., McCoy, T.J., Boynton, W.V., Gillis-Davis, J.J., Ebel, D.S., Goldsten, J.O., Hamara, D.K., Lawrence, D.J., McNutt, R.L., Nittler, L.R., Solomon, S.C., Rhodes, E.A., Sprague, A.L., Starr, R.D., Stockstill-Cahill, K.R., 2011. Radioactive elements on Mercury's surface from MESSENGER: implications for the planet's formation and evolution. Science 333, 1850–1852.
Peplowski, P.N., Evans, L.G., Rhodes, E.A., Goldsten, J.O., Hamara, D.K., Head, J.W., Lawrence, D.J., Nittler, L.R., Solomon, S.C., Sprague, A.L., 2012, December. Elemental composition of the surface of mercury from the MESSENGER gamma-ray spectrometer. In: AGU Fall Meeting Abstracts (Vol. 2012, pp. P31D-05).
Peplowski, P.N., Evans, L.G., Stockstill-Cahill, K.R., Lawrence, D.J., Goldsten, J.O., McCoy, T.J., Nittler, L.R., Solomon, S.C., Sprague, A.L., Starr, R.D., Weider, S.Z., 2014. Enhanced sodium abundance in Mercury's north polar region revealed by the MESSENGER Gamma-Ray Spectrometer. Icarus 228, 86–95.
Peplowski, P.N., Lawrence, D.J., Feldman, W.C., Goldsten, J.O., Bazell, D., Evans, L.G., Head, J.W., Nittler, L.R., Solomon, S.C., Weider, S.Z., 2015. Geochemical terranes of

Mercury's northern hemisphere as revealed by MESSENGER neutron measurements. Icarus 253, 346–363.
Peterson, G.A., Johnson, C.L., Jellinek, A.M., 2021. Thermal evolution of mercury with a volcanic heat-pipe flux: reconciling early volcanism, tectonism, and magnetism. Science. Advances 7 (40), eabh2482.
Rivoldini, A., Van Hoolst, T., 2013. The interior structure of Mercury constrained by the low-degree gravity field and the rotation of Mercury. Earth Planet. Sci. Lett. 377–378, 62–72.
Rothery, D.A., Massironi, M., Alemanno, G., Barraud, O., Besse, S., Bott, N., Brunetto, R., Bunce, E., Byrne, P., Capaccioni, F., Capria, M.T., Carli, C., Charlier, B., Cornet, T., Cremonese, G., D'Amore, M., De Sanctis, M.C., Doressoundiram, A., Ferranti, L., Filacchione, G., Galluzzi, V., Giacomini, L., Grande, M., Guzzetta, L.G., Helbert, J., Heyner, D., Hiesinger, H., Hussmann, H., Hyodo, R., Kohout, T., Kozyrev, A., Litvak, M., Lucchetti, A., Malakhov, A., Malliband, C., Mancinelli, P., Martikainen, J., Martindale, A., Maturilli, A., Milillo, A., Mitrofanov, I., Mokrousov, M., Morlok, A., Muinonen, K., Namur, O., Nittler, L.R., Oliveira, J.S., Owens, A., Palumbo, P., Pajola, M., Pegg, D.L., Penttilä, A., Politi, R., Quarati, F., Re, C., Sanin, A., Schulz, R., Stangarone, C., Stojic, A., Tretiyakov, V., Väisänen, T., Varatharajan, I., Weber, I., Wright, J., Wurz, P., Zambon, F., 2020. Rationale for BepiColombo Studies of Mercury's Surface and composition. Space Sci. Rev. 216, 1–46.
Shannon, R.D., 1976. Revised effective ionic radii and systematic studies of interatomic distances in halides and chalcogenides. Acta Crystallogr. Sec. A 32, 751–767.
Shaw, D.M., 1970. Trace element fractionation during anatexis. Geochim. Cosmochim. Acta 34 (2), 237–243.
Smith, D.E., Zuber, M.T., Phillips, R.J., Solomon, S.C., Hauck, S.A., Lemoine, F.G., Mazarico, E., Neumann, G.A., Peale, S.J., Margot, J.-L., Johnson, C.L., Torrence, M. H., Perry, M.E., Rowlands, D.D., Goossens, S., Head, J.W., Taylor, A.H., 2012. Gravity field and internal structure of Mercury from MESSENGER. Science 336, 214–217.
Steenstra, E.S., Agmon, N., Berndt, J., Klemme, S., Matveev, S., van Westrenen, W., 2018. Depletion of potassium and sodium in mantles of Mars, Moon and Vesta by core formation. Sci. Rep. 8 (1), 7053.
Steenstra, E.S., Trautner, V.T., Berndt, J., Klemme, S., van Westrenen, W., 2020a. Trace element partitioning between sulfide-, metal- and silicate melts at highly reduced conditions: insights into the distribution of volatile elements during core formation in reduced bodies. Icarus 335, 113408.
Steenstra, E.S., Kelderman, E., Berndt, J., Klemme, S., Bullock, E.S., van Westrenen, W., 2020b. Highly reduced accretion of the Earth by large impactors? Evidence from elemental partitioning between sulfide liquids and silicate melts at highly reduced conditions. Geochim. Cosmochim. Acta 286, 248–268.
Steinbrügge, G., Dumberry, M., Rivoldini, A., Schubert, G., Cao, H., Schroeder, D.M., Soderlund, K.M., 2021. Challenges on Mercury's interior structure posed by the new measurements of its obliquity and tides. Geophys. Res. Lett. 48 (3).
Thibault, Y., Walter, M.J., 1995. The influence of pressure and temperature on the metal-silicate partition coefficients of nickel and cobalt in a model C1 chondrite and implications for metal segregation in a deep magma ocean. Geochim. Cosmochim. Acta 59 (5), 991–1002.
Tosi, N., Grott, M., Plesa, A.C., Breuer, D., 2013. Thermochemical evolution of Mercury's interior. J. Geophys. Res. Planets 118, 2474–2487.
van Achterbergh, E., Ryan, C., Jackson, S., Griffin, W., 2001. Data reduction software for LA-ICP-MS. In: Sylvester, P. (Ed.), Laser Ablation-ICPMS in the Earth Sciences, Mineral Assoc Can Short Course Handbook, vol. 29, pp. 239–243.
Vander Kaaden, K.E., McCubbin, F.M., 2016. The origin of boninites on Mercury: an experimental study of the northern volcanic plains lavas. Geochim. Cosmochim. Acta 173, 246–263.
Vander Kaaden, K.E., McCubbin, F.M., Turner, A.A., Ross, D.K., 2020. Constraints on the abundances of carbon and silicon in Mercury's core from experiments in the Fe-Si-C system. J. Geophys. Res. Planets 125 (5) e2019JE006239.
Wasson, J.T., Kallemeyn, G.W., 1988. Compositions of chondrites. Philos. Trans. R. Soc. Lond. A Math. Phys. Sci. 325 (1587), 535–544.
Weider, S.Z., Nittler, L.R., Starr, R.D., Crapster-Pregont, E.J., Peplowski, P.N., Denevi, B. W., Head, J.W., Byrne, P.K., Hauck Ii, S.A., Ebel, D.S., Solomon, S.C., 2015. Evidence for geochemical terranes on Mercury: global mapping of major elements with MESSENGER's X-ray spectrometer. Earth Planet. Sci. Lett. 416, 109–120.
Wiik, H.B., 1956. The chemical composition of some stony meteorites. Geochim. Cosmochim. Acta 9, 279–289.
Wilbur, Z.E., Udry, A., McCubbin, F.M., vander Kaaden, K.E., DeFelice, C., Ziegler, K., Ross, D.K., McCoy, T.J., Gross, J., Barnes, J.J., Dygert, N., 2022. The effects of highly reduced magmatism revealed through aubrites. Meteorit. Planet. Sci. 57 (7), 1387–1420.
Wipperfurth, S.A., Guo, M., Šrámek, O., McDonough, W.F., 2018. Earth's chondritic Th/U: negligible fractionation during accretion, core formation, and crust–mantle differentiation. Earth Planet. Sci. Lett. 498, 196–202.
Wohlers, A., Wood, B.J., 2015. A Mercury-like component of early Earth yields uranium in the core and high mantle 142Nd. Nature 520, 337–340.
Wohlers, A., Wood, B.J., 2017. Uranium, thorium and REE partitioning into sulfide liquids: implications for reduced S-rich bodies. Geochim. Cosmochim. Acta 205, 226–244.
Wood, B.J., Kiseeva, E.S., 2015. Trace element partitioning into sulfide: how lithophile elements become chalcophile and vice versa. Am. Mineral. 100, 2371–2379.
Zolotov, M.Y., Sprague, A.L., Hauck, S.A., Nittler, L.R., Solomon, S.C., Weider, S.Z., 2013. The redox state, FeO content, and origin of sulfur-rich magmas on Mercury. J. Geophys. Res. Planets 118, 138–146.